Journal of Volcanology and Geothermal Research 323 (2016) 148–162

Contents lists available at ScienceDirect

Journal of Volcanology and Geothermal Research

journal homepage: www.elsevier.com/locate/jvolgeores

Reconstructing CO_2 concentrations in basaltic melt inclusions using Raman analysis of vapor bubbles

Ellen M. Aster [a,*], Paul J. Wallace [a], Lowell R. Moore [b], James Watkins [a], Esteban Gazel [b], Robert J. Bodnar [b]

[a] Department of Geological Sciences, University of Oregon, Eugene, OR 97403, USA
[b] Department of Geosciences, Virginia Tech, Blacksburg, VA 24061, USA

ARTICLE INFO

Article history:
Received 30 August 2015
3 March 2016
Accepted 28 April 2016
Available online 03 May 2016

Keywords:
Vapor bubbles
Melt inclusions
Volatiles
Raman spectroscopy

ABSTRACT

Melt inclusions record valuable information about pre-eruptive volatile concentrations of melts. However, a vapor bubble commonly forms in inclusions after trapping, and this decreases the dissolved CO_2 concentration in the melt (glass) phase in the inclusion. To quantify CO_2 loss to vapor bubbles, Raman spectroscopic analysis was used to determine the density of CO_2 in bubbles in melt inclusions from two Cascade cinder cones near Mt. Lassen and two Mexican cinder cones (Jorullo, Parícutin). Using analyses of dissolved CO_2 and H_2O in the glass in the inclusions, the measured CO_2 vapor densities were used to reconstruct the original dissolved CO_2 contents of the melt inclusions at the time of trapping. Our results show that 30–90% of the CO_2 in a melt inclusion is contained in the vapor bubble, values similar to those found in other recent studies. We developed a model for vapor bubble growth to show how post-entrapment bubbles form in melt inclusions as a result of cooling, crystallization, and eruptive quenching. The model allows us to predict the bubble volume fraction as a function of ΔT (the difference between the trapping temperature and eruptive temperature) and the amount of CO_2 lost to a bubble. Comparison of the Raman and modeling methods shows highly variable agreement. For 10 of 17 inclusions, the two methods are within $\pm$550 ppm CO_2 (avg. difference 290 ppm), equivalent to $\pm$~300 bars uncertainty in estimated trapping pressure for restored inclusions. Discrepancies between the two methods occur for inclusions that have been strongly affected by post-entrapment diffusive H^+ loss, because this process enhances bubble formation. For our dataset, restoring the CO_2 lost to vapor bubbles increases inferred trapping pressures of the inclusions by 600 to as much as 4000 bars, highlighting the importance of accounting for vapor bubble formation in melt inclusion studies.

1. Introduction

Melt inclusions are small volumes of melt trapped within a crystallizing phenocryst. Because melt inclusions sequester melt prior to eruptive degassing, they provide a useful record of volatile concentrations in melts during crystallization (e.g. Lowenstern, 1995; Metrich and Wallace, 2008). However, during post-entrapment cooling and crystallization most melt inclusions undergo a decrease in pressure, unless the melt is H_2O-saturated, in which case pressure can increase (e.g., Student and Bodnar, 1996). The pressure decrease causes nucleation of a vapor bubble and loss of volatiles from the melt into the bubble (Anderson and Brown, 1993; Steele-MacInnis et al., 2011; Moore et al., 2015; Wallace et al., 2015). The pressure drop within a melt inclusion has a particularly strong effect on CO_2 because of the strong pressure dependence of CO_2 solubility.

There are several factors that contribute to the post-entrapment pressure drop within a melt inclusion. First, cooling causes crystallization of the included melt at the inclusion-host interface (Steele-MacInnis et al., 2011; Wallace et al., 2015). Because the phase transition from silicate melt to solid (e.g., olivine) results in a volume decrease, post-entrapment crystallization causes a pressure drop within a melt inclusion, leading to nucleation and growth of a vapor bubble (Lowenstern, 1995; Danyushevsky et al., 2002). Second, the cooling that causes crystallization also causes the melt to contract more than the olivine host because of the difference in thermal expansivity of the two phases (Sorby, 1858; Roedder, 1979). During eruption, cooling from the pre-eruptive temperature to quenching at the glass transition temperature causes additional contraction of the melt (Anderson and Brown, 1993; Riker, 2005). Cooling during eruption may occur on a timescale that is too short for significant diffusion of dissolved CO_2 from the melt into the vapor bubble, but it does promote an increase in vapor bubble size (Anderson and Brown, 1993; Wallace et al., 2015). Third, diffusive loss of H^+ (protons) out of a melt inclusion (Hauri, 2001; Gaetani et al., 2012; Bucholz et al., 2013) can also increase bubble size because this process causes an increase in melt density and a decrease in melt mass in the inclusion. These post-entrapment processes all act to reduce the dissolved CO_2 concentration in a melt inclusion, making it difficult to infer the original crystallization pressure of the host crystal based on vapor saturation calculations using dissolved H_2O and CO_2 in the

* Corresponding author.
E-mail address: astere@oregonstate.edu (E.M. Aster).

http://dx.doi.org/10.1016/j.jvolgeores.2016.04.028
0377-0273/

Table 1
Volume percent vapor bubble, CO_2 densities in the bubble determined by Raman, and H_2O and CO_2 concentrations in the glass determined by FTIR.

Inclusion	Bub. vol.%	CO_2 Density (g/cm^3)	Carb.	Measured CO_2 ppm	CO_2 Uncertainty ppm	Measured H_2O wt.%	H_2O Uncertainty wt.%	EPMA
Basalt of Old Railroad Grade (BORG-1)								
2.2	6	0.17	–	–	–	–	–	–
2.3	5	0.18	–	–	–	–	–	–
3.2	3	0.10	X	–	–	–	–	–
3.3	3	0.07	X	–	–	–	–	–
3.4	7	0.07	X	–	–	–	–	–
5.2	1	0.16	X	1141	±207*	2.4	±0.3*	X
6.2	1	0.15	–	306	±32	0.8	±0.03	–
6.3	1	0.14	–	–	–	–	–	–
6.4	1	0.14	X	–	–	–	–	–
6.5	2	0.24	X	–	–	–	–	–
9.3	2	0.11	X	–	–	–	–	–
9.4	6	0.12	X	–	–	–	–	–
10.2	2	0.23	–	1249	±208*	1.1	±0.67*	–
10.3	3	0.05	–	–	–	–	–	–
11.2	7	0.10	X	–	–	–	–	–
12.2	2	0.14	X	–	–	–	–	–
12.3	1	0.14	X	–	–	–	–	–
12.4	1	0.13	X	–	–	–	–	–
12.5	2	0.14	X	–	–	–	–	–
13.2	2	0.14	–	1188	±43	2.1	±0.01	–
15.2	3	0.14	X	–	–	–	–	–
15.d	3	0.12	X	–	–	–	–	–
15.h	4	0.11	X	–	–	–	–	–
18.1	1	0.12	X	–	–	–	–	–
19.2	2	0.13	X	688	±323*	1.9	±0.2*	X
19.4	4	0.17	–	–	–	–	–	–
19.5	3	0.13	–	559	±559*	1.7	±0.4*	X
19.8	2	0.14	X	1443	±444*	1.8	±0.7*	X
19.h	4	0.14	–	–	–	–	–	–
19.i	4	0.14	–	–	–	–	–	–
19.l	3	0.12	X	–	–	–	–	–
19.n	3	0.13	–	–	–	–	–	–
19.s	4	0.15	X	–	–	–	–	–
20.1	3	0.13	X	–	–	–	–	–
21.2	2	0.16	X	–	–	–	–	–
22.3	2	0.14	–	b.d.	N/A	b.d.	N/A	X
23.1	2	0.13	–	761*	±52	1.3*	±0.4	X
24.1	2	0.17	–	320	±46	0.9	±0.03	X
26.1	2	0.10	X	–	–	–	–	–
26.4	1	0.11	–	–	–	–	–	–
26.b	2	0.08	X	–	–	–	–	–
27.2	4	0.14	–	880	±45	1.7	±0.4	X
27.3	2	0.16	X	–	–	–	–	–
27.b	4	0.14	–	–	–	–	–	–
27.c	4	0.16	–	–	–	–	–	–
30.a	3	0.22	–	–	–	–	–	–
32.a	6	0.14	–	b.d.	N/A	0.9	±0.5	X
33.3	3	0.14	X	303	±57	0.7	±0.03	X
Basalt of Round Valley Butte (BRVB-01)								
2.2	5	0.13	–	–	–	–	–	–
2.3	3	0.13	–	–	–	–	–	–
2.7	5	0.10	X	–	–	–	–	–
4.4	7	0.19	–	–	–	–	–	–
4.6	4	0.20	–	–	–	–	–	–
4.7	4	0.21	–	–	–	–	–	–
4.8	7	0.11	–	–	–	–	–	–
4.9	7	0.19	–	–	–	–	–	–
5.2	5	0.21	–	–	–	–	–	–
6.4	2	0.23	X	–	–	–	–	–
6.5	3	0.24	–	–	–	–	–	–
6.6	3	0.21	X	–	–	–	–	–
6.7	1	0.20	X	–	–	–	–	–
6.8	4	0.23	–	–	–	–	–	–
6.9	2	0.27	–	–	–	–	–	–
8.2	4	0.15	–	–	–	–	–	–
8.4	3	0.24	–	–	–	–	–	–
10.3	8	0.13	–	–	–	–	–	–
11.2	4	0.10	–	–	–	–	–	–
11.3	5	0.13	–	–	–	–	–	–
11.4	2	0.12	–	–	–	–	–	–
11.5	3	0.07	–	–	–	–	–	–
12.3	3	0.29	–	–	–	–	–	–
13.2	6	0.21	–	–	–	–	–	–

(continued on next page)

Table 1 (*continued*)

Inclusion	Bub. vol.%	CO_2 Density (g/cm^3)	Carb.	Measured CO_2 ppm	CO_2 Uncertainty ppm	Measured H_2O wt.%	H_2O Uncertainty wt.%	EPMA
14.2	9	0.22	–	–	–	–	–	–
14.3	9	0.23	–	–	–	–	–	–
18.3	6	0.17	–	608	±43	0.1	±0.01	X
19.3	4	0.24	–	–	–	–	–	–
21.a	6	0.23	–	–	–	–	–	–
21.b	3	0.17	–	–	–	–	–	–
21.d	3	0.20	–	–	–	–	–	–
21.f	4	0.22	–	–	–	–	–	–
21.g	3	0.11	–	–	–	–	–	–
21.h	5	0.24	–	–	–	–	–	–
22.1	3	0.12	–	–	–	–	–	–
22.2	4	0.17	–	–	–	–	–	–
24.2	2	0.24	X	b.d.	N/A	1.6	±0.8*	X
27.1	3	0.09	–	–	–	–	–	–
27.d	2	0.18	–	–	–	–	–	–
27.e	13	0.16	–	–	–	–	–	–
29.a	3	0.09	–	–	–	–	–	–
29.b	7	0.12	–	–	–	–	–	–
30.1	7	0.23	–	803	±732*	0.4	±0.06*	–
30.a	8	0.24	–	–	–	–	–	–
31.3	–	–	–	905	±150	1.2	±0.14	X
36.1	2	0.13	–	–	–	–	–	–
37.1	4	0.07	–	b.d.	N/A	0.4	±0.04	X
39.1	–	–	–	618	±207*	1.2	±0.31*	–
40.1	1	0.19	–	–	–	–	–	–
Jorullo (J1d)								
4.c	7	0.18	–	–	–	–	–	–
6.a	14	0.13	–	–	–	–	–	–
6.b	8	0.15	–	–	–	–	–	–
7.a	10	0.14	–	897	±350*	0.6	±0.48*	–
7.d	10	0.08	X	–	–	–	–	–
7.f	13	0.12	–	–	–	–	–	–
7.h	15	0.12	–	–	–	–	–	–
7.l	6	0.18	–	–	–	–	–	–
7.m	9	0.15	–	–	–	–	–	–
8.1	8	0.20	–	712	±115	1.9	±0.14	–
9.1	6	0.21	–	–	–	–	–	–
10.1	6	0.18	–	–	–	–	–	–
11.c	6	0.04	X	–	–	–	–	–
12.c	6	0.09	–	–	–	–	–	–
13.2	13	0.17	–	–	–	–	–	–
14.1	–	–	–	532	±100	2.6	±0.17	X
18.a	7	0.04	X	–	–	–	–	–
20.1	4	0.05	X	654	±76	2.8	±0.3	X
20.a	6	0.03	X	–	–	–	–	–
Parícutin (P506)								
1.1	–	–	–	328	±18*	1.4	±0.1*	X
3.2	2	0.06	–	–	–	–	–	–
3.a	4	0.09	–	–	–	–	–	–
4.1	4	0.02	–	–	–	–	–	–
7.1	3	0.07	–	794	±61	1.6	±0.3	X
8.1	7	0.12	–	–	–	–	–	–
10.1	2	0.08	–	446	±24*	1.4	±0.08*	–
11.1	–	–	–	514	±142*	1.3	±0.3*	–
12.1	–	–	–	509	N/A	0.8	N/A	X
15.1	5	0.02	–	–	–	–	–	–
15.b	6	0.06	–	–	–	–	–	–
15.c	9	0.05	–	–	–	–	–	–
17.1	–	–	–	1136	±359*	1.5	±0.14*	–
17.a	9	0.05	–	–	–	–	–	–

The uncertainty in CO_2 density is ±0.02 g/cm^3 (1 standard deviation); we estimated uncertainty in CO_2 density measurements using the deviation in CO_2 densities from repeated Raman analyses of a vapor bubble in a BRVB inclusion, as described in Section 2.2. Uncertainty in glass CO_2 and H_2O concentrations were calculated as explained in Section 2.3. H_2O and CO_2

melt (glass) (Anderson and Brown, 1993; Steele-MacInnis et al., 2011; Moore et al., 2015; Wallace et al., 2015; Mironov et al., 2015).

To investigate the effect of vapor bubble formation on the dissolved CO_2 concentration in olivine-hosted melt inclusions from mafic cinder cones in volcanic arcs, we employed a combination of analytical and modeling techniques. Following the methods first described in Esposito et al. (2011) and recently detailed in Moore et al. (2015), we used Raman spectroscopy to measure the CO_2 gas density in bubbles in melt inclusions from four cinder cones: two from the southern Cascade Arc (Basalt of Round Valley Butte [BRVB] and Basalt of Old Railroad Grade [BORG]; Clynne and Muffler, 2010; Walowski, in review; Walowski et al., 2016) and two historically active cinder cones from Mexico (Jorullo and Parícutin; Johnson et al., 2009). We used bubble volumes, bubble CO_2 densities, and CO_2 concentrations in melt

inclusion glasses measured by Fourier transform infrared (FTIR) spectroscopy to quantify the amount of CO_2 that was lost from the melt to the bubble in the inclusion (Moore et al., 2015). To distinguish bubbles that were likely co-entrapped with melt from bubbles that formed post-entrapment, we calculated the maximum bubble volume fraction that could have formed post-entrapment for melt inclusions from each volcano based on differences between eruptive and trapping temperatures (Riker, 2005; Wallace et al., 2015). We compared Raman-reconstructed CO_2 concentrations to CO_2 reconstructions calculated using a model of post-entrapment crystallization and melt contraction to assess the agreement between the two approaches. Using these results together with estimates of the extent of diffusive H^+ loss, we reconstructed pressures of entrapment for melt inclusions from each volcano.

2. Methods

2.1. Sample description and preparation

Loose olivine phenocrysts were selected from tephra samples collected by K. Walowski (BORG; BRVB) and E. Johnson (Jorullo; Parícutin) to minimize the probability of selecting melt inclusions affected by syn- or post-eruptive diffusive loss due to slow cooling (Lloyd et al., 2013). Bulk tephra from each volcano was sieved into different size fractions. The 250 μm–500 μm and 500 μm–1 mm fractions contained the largest proportion of euhedral olivine phenocrysts with the least amount of adhering matrix glass so that the phenocrysts could be easily inspected for melt inclusions using a stereomicroscope. Phenocrysts were immersed in isopropyl alcohol and placed under a microscope for selection of olivine containing fully enclosed, glassy melt inclusions without fractures. Olivine phenocrysts were then mounted onto round glass slides using an acetone-soluble resin. To prepare for Raman analysis, mounted samples were polished using 6 and 1/4 μm diamond grit until at least one melt inclusion with a bubble was close enough (<100 μm) to the surface to be analyzed by Raman spectroscopy.

The volume of each bubble and melt inclusion was calculated using the open-source program ImageJ (Abramoff et al., 2004) after measuring the dimensions of the melt inclusion and bubble on a photo. We calculated a spherical volume for each bubble and an ellipsoidal volume for each melt inclusion. For each ellipsoidal melt inclusion volume, we assumed that the third, unobservable ellipsoidal axis (extending in and out of the plane of the photo) was approximated by the smaller ellipsoidal axis measured on the photograph. Although this is not ideal, this was the best estimate for the third axis using two-dimensional photos. Bubble volume % values for the inclusions are given in Table 1.

Olivines from BORG contain only a few mineral inclusions and usually more than one ellipsoidal melt inclusion per crystal. Of the 249 bubbles analyzed by Raman spectroscopy in BORG melt inclusions, 19 bubbles are in melt inclusions with a 'wrinkled' texture (see Fig. A1 in Appendix A, and Fig. 3d in Moore et al., 2015). The rest of the analyses were of bubbles in smooth-walled inclusions. Most of the smooth-walled melt inclusions in BORG olivine are colorless, with only a few transparent light brown inclusions. The melt inclusions in BORG olivine have bubble volumes ranging from 0.9 to 6.7 vol.% (avg. 2.9%) of the total melt inclusion volume (Fig. 1).

BRVB olivines contain numerous mineral inclusions as well as many ellipsoidal to faceted (negative crystal shape) melt inclusions (see Fig. A2 in Appendix A). The melt inclusions all have smooth walls and are transparent tan in color. Eleven of the 143 bubbles analyzed by Raman are in melt inclusions that contain a small unidentified crystal; the rest of the inclusions are crystal-free. BRVB bubble volumes range from 1.3 to 13 vol.% bubble (avg. 4.5%).

Jorullo olivines contain numerous mineral inclusions in addition to melt inclusions, and the melt inclusions are typically faceted (negative crystal shape) rather than ellipsoidal (see Fig. A3 in Appendix A). The inclusions are smooth-walled, with colors ranging from colorless to transparent tan. Four of the 81 analyzed bubbles are in melt inclusions that contain small (~3–10 μm) unidentified crystals either within the melt inclusion glass or along the inclusion-host interface. The rest of the melt inclusions in which bubbles were analyzed do not contain crystals. Jorullo melt inclusions have the largest average bubble volume fractions, ranging from 3.9 to 15 vol.% (avg. 8.5%).

Parícutin olivines contain many round to faceted (negative crystal shape) melt inclusions and reentrants (see Fig. A4 in Appendix A). Numerous mineral inclusions are also observed in the olivine. Parícutin olivines contain the largest melt inclusions of the three volcanoes (Fig. 1). Of the 54 bubbles analyzed by Raman, four are in inclusions that contain small unidentified crystals. Four of the analyzed melt inclusions contain more than one bubble; however, during Raman analysis, no CO_2 was detected in any of these multiple bubbles. For Parícutin, bubble volume percent ranges from 1.7 to 8.8 vol.% bubble (avg. 5.1%).

2.2. Raman spectroscopy

The density of CO_2 in vapor bubbles in melt inclusions was determined at Virginia Tech on a JY Horiba LabRam HR (800) Raman spectrometer (see Esposito et al., 2011, Moore et al., 2015). Analyses were conducted using a 400-μm diameter confocal hole and a 150-μm slit. The instrument uses a Modu-Laser 514 argon laser set at 50 mW at the source, with Raman shifted photons diffracted by an 1800 grooves/mm grating to an Andor electronically cooled CCD detector. A synthetic fluid inclusion containing a low-density CO_2 vapor bubble (Sterner and Bodnar, 1984) and a vapor bubble in a melt inclusion from BRVB were analyzed three times a day to test for reproducibility of Raman analyses. Five 30-second accumulations (150 s total) were obtained for the melt inclusion bubbles and the reference standards. The background for each sample was corrected for noise using LabSpec software, and peaks were fit using a mixed Gaussian/Lorentzian approximation with Grams/AI™ Spectroscopy Software (by Thermo Scientific). Spectra containing CO_2 peaks that are too small to be recognized by the peak fitting software (usually corresponding to "peaks" defined by 4 or fewer points) were noted but not included in the final dataset.

The density of CO_2 in each bubble was calculated using the difference in wavenumber between two characteristic peaks, called the Fermi diad, located at ~1285.4 cm^{-1} and 1388.2 cm^{-1} (Wright and Wang, 1973, 1975). As CO_2 density increases, the peaks of the Fermi diad shift farther apart. The density of CO_2 can be calculated using:

$$\rho_{CO_2} = -0.0303\Delta^3 + 9.43\Delta^2 - 977.398\Delta + 33780.382 \quad (1)$$

where ρ_{CO_2} is the density of CO_2 (g/cm^3) and Δ is the difference in wavenumber (cm^{-1}) between the two peaks in the Fermi diad (Fall et al., 2011). This density relationship was calibrated at Virginia Tech using the same Raman system and procedures that we used, and the calibration includes many data points in the low-density (vapor) region, which is appropriate for bubbles in melt inclusions. In some melt inclusions carbonate crystals are present along the bubble-inclusion wall (e.g., Moore et al., 2015). These crystals produce a Raman peak at ~1100 cm^{-1}. Because an unquantifiable amount of CO_2 is contained in the carbonate, bubbles that had carbonate were noted. Measured CO_2 densities are reported in Table 1, and bubbles with carbonate present are also noted.

2.3. Fourier transform infrared (FTIR) spectroscopy

After the bubbles were analyzed by Raman spectroscopy, melt inclusions were prepared for analysis of H_2O and CO_2 concentrations in the glass phase using a Thermo Nicolet Nexus 670 Fourier transform infrared (FTIR) spectrometer at the University of Oregon. Each olivine

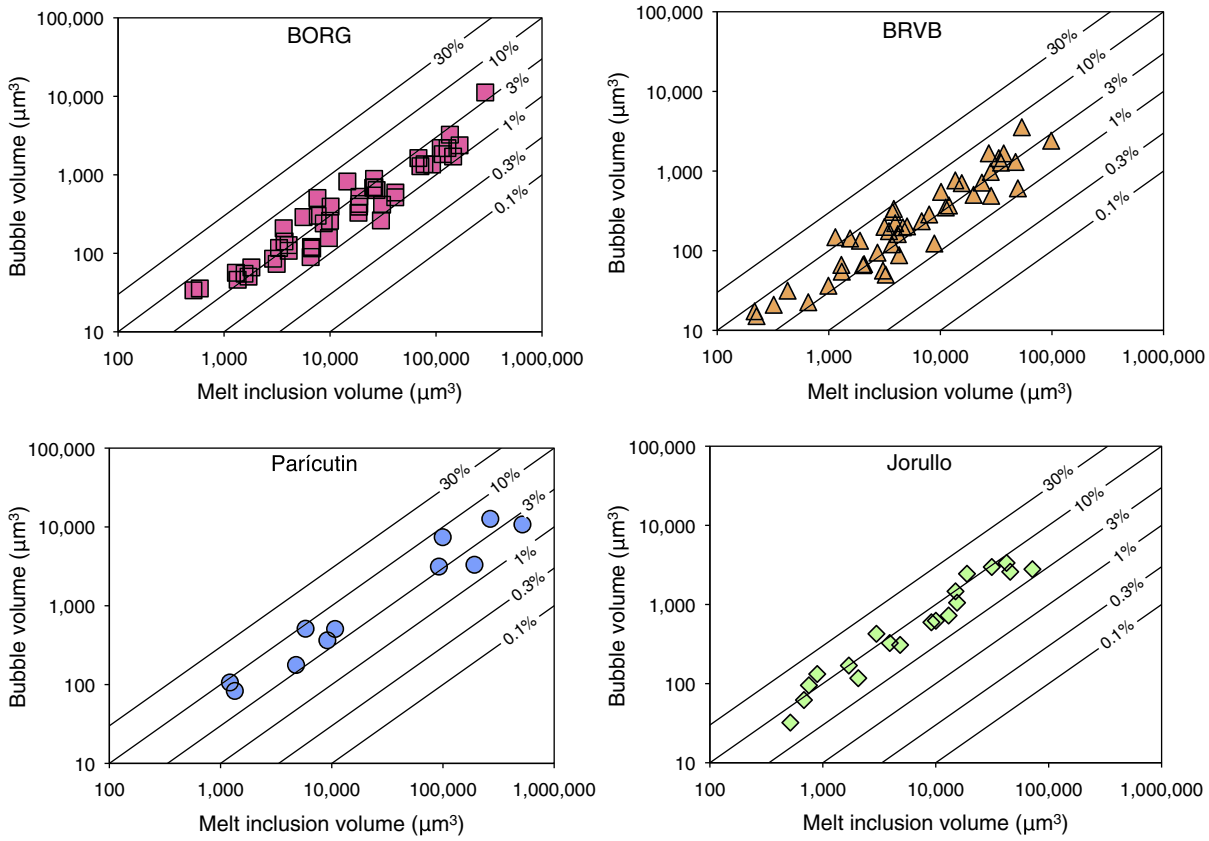

Fig. 1. Comparison of melt inclusion volumes and vapor bubble volumes. Isovolumetric lines representing volume percent vapor in the melt inclusion are also shown. Bubble volumes for all analyzed samples ranged from ~1–10 vol.%.

grain was ground and polished into a wafer using 6 and 1/4 μm diamond grit so that melt inclusions were intersected on two sides. Olivine wafer thicknesses were measured using both a digital micrometer and with interference fringes in reflectance spectra (Wysoczanski and Tani, 2006). Some melt inclusions, due to fragility of the thin wafer and their small (<30 μm in diameter) size, were not doubly intersected. For these melt inclusions, measured thicknesses were corrected for the presence of olivine (Nichols and Wysoczanski, 2007).

Three transmission spectra were collected from each melt inclusion glass. H_2O and CO_2 concentrations were then calculated from each spectrum using Beer's Law:

$$c = MA/\rho d\varepsilon \quad (2)$$

where c is the concentration of H_2O or CO_2 (in weight fraction), M is the molecular weight of H_2O or CO_2, A is the measured absorbance for total H_2O using the fundamental O–H stretching vibration (peak at 3550 cm^{-1}), or carbonate (doublet at 1515 and 1430 cm^{-1}); ρ is the glass density; d is the thickness of the melt inclusion (μm); and ε is the molar absorption coefficient. For all melt inclusions we used $\varepsilon_{H_2O} = 63$ L/mol cm (Dixon et al., 1995). The value for ε_{CO_2}, however, is sensitive to melt composition, and we used an average melt inclusion composition from each cone to calculate the following values: $\varepsilon_{CO_2} =$ 308 L/mol cm for BORG, 310 L/mol cm for BRVB, 291 L/mol cm for Jorullo, and 280 L/mol cm for Parícutin (Dixon and Pan, 1995). The absorbance of CO_2 as carbonate was measured using a peak-fitting program that uses a background subtraction of carbonate-free basaltic glass (S. Newman, unpublished). Glass densities at 1 bar and 25 °C were calculated using major element compositions and partial molar volumes from R. Lange (cited in Luhr, 2001). Analytical uncertainties in CO_2 and H_2O concentrations for each melt inclusion were determined by propagating error from thickness measured by reflectance spectra, absorbance, and (for small melt inclusions) thickness after correcting for the presence of olivine in the spectra.

2.4. Electron microprobe analysis

Major element concentrations in melt inclusions (Si, Al, Fe, Mg, Ca, Na, K, Mn, Ti, P) and host olivine (Si, Mg, Fe, Mn) were determined using a Cameca SX-100 electron microprobe at the University of Oregon. SiO_2, Al_2O_3, Na_2O, and K_2O were analyzed first, and concentrations were determined using time-dependent intensity corrections. Five points on each melt inclusion and three points on each olivine were analyzed with a 2-μm beam diameter, 15 kV accelerating voltage, and a sample current of 20 nA.

Melt inclusion compositions were corrected for diffusive Fe loss (Danyushevsky et al., 2000) and post-entrapment crystallization (PEC) of olivine along the melt inclusion-olivine interface using Petrolog3 (Danyushevsky and Plechov, 2011). For the correction, we used an oxygen fugacity determined from V partitioning between olivine and melt (Mallmann and O'Neill, 2009), which yielded an average value of QFM + 1. In Petrolog3, olivine-melt K_d values were calculated using Danyushevsky (2001). We used FeO^T values based on corrected melt inclusion FeO^T data [Jorullo restored FeO^T = 7.51 wt.%, Parícutin restored FeO^T = 7.18 wt.% (Johnson et al., 2009)], and whole rock data [BORG restored FeO^T = 8.54 wt.%, BRVB restored FeO^T = 9.39 wt.% (Walowski, 2015; Walowski et al., 2016)]. After restoring melt inclusion major element values, we corrected for the effects of PEC on volatile concentrations. Because K is incompatible during olivine crystallization, the ratio of uncorrected K_2O to corrected K_2O for each volcano was used to correct the CO_2 and H_2O values. Measured and corrected electron microprobe compositions along with measured and corrected H_2O and CO_2 concentrations for each melt inclusion are given in Table 2.

Table 2
Major elements, volatiles, and ΔT for melt inclusions analyzed by electron microprobe.

Uncorrected	BORG-1									
	5.2	19.2	19.5	19.8	22.3	23-1	24.1	27.2	32.a	33.3
SiO_2	49.46	48.18	48.51	49.85	49.31	50.35	48.46	51.21	50.88	47.66
TiO_2	0.92	0.89	0.95	0.95	0.88	1.15	0.76	0.97	0.88	0.77
Al_2O_3	20.28	21.57	21.46	20.79	19.63	19.89	19.32	20.33	19.40	20.10
FeO^T	6.05	6.52	5.96	6.43	8.47	7.58	6.57	6.54	7.22	7.82
MnO	0.09	0.12	0.08	0.10	0.13	0.12	0.10	0.12	0.12	0.13
MgO	4.06	4.34	4.63	4.90	5.61	3.74	6.95	3.28	4.50	5.75
CaO	11.59	10.00	9.99	9.93	9.56	9.39	11.47	9.98	9.32	10.64
Na_2O	3.39	4.54	4.63	4.89	3.99	4.19	3.15	4.44	4.18	3.17
K_2O	0.60	0.59	0.65	0.65	0.51	0.64	0.54	0.63	0.59	0.46
P_2O_5	0.27	0.23	0.22	0.22	0.22	0.26	0.23	0.24	0.23	0.20
H_2O	2.4	1.9	1.7	1.8	b.d.	1.3	0.9	1.7	0.9	0.7
H_2O uncertainty	±0.3*	±0.2*	±0.4*	±0.7*	N/A	±0.4*	±0.03	±0.4	±0.5	±0.03
CO_2 ppm	1141	688	559	1443	b.d.	761	320	880	b.d.	303
CO_2 uncertainty	±207*	±323*	±289*	±444*	N/A	±52*	±46	±45	N/A	±57

Corrected	BORG-1									
	5.2	19.2	19.5	19.8	22.3	23.1	24.1	27.2	32.a	33.3
SiO_2	49.14	48.46	48.49	49.26	50.10	50.83	48.54	50.73	51.30	48.77
TiO_2	0.81	0.83	0.87	0.89	0.90	1.11	0.71	0.88	0.85	0.76
Al_2O_3	17.76	20.12	19.66	19.30	19.95	19.12	18.08	18.47	18.72	19.87
Fe_2O_3	1.05	1.21	1.23	1.33	1.40	1.28	1.11	1.22	1.29	1.10
FeO	7.77	7.62	7.58	7.53	7.28	7.51	7.63	7.58	7.55	7.67
MnO	0.13	0.15	0.12	0.13	0.13	0.15	0.13	0.15	0.14	0.15
MgO	9.35	7.21	7.79	6.94	5.72	6.03	9.35	6.99	6.28	7.35
CaO	10.25	9.39	9.22	9.28	9.71	9.08	10.79	9.15	9.03	10.55
Na_2O	2.97	4.24	4.24	4.54	4.06	4.03	2.95	4.04	4.04	3.13
K_2O	0.53	0.55	0.60	0.60	0.52	0.62	0.51	0.57	0.57	0.45
P_2O_5	0.24	0.22	0.20	0.20	0.22	0.25	0.22	0.22	0.22	0.20
H_2O	2.0	1.7	1.5	1.6	b.d.	1.3	0.8	1.5	0.8	0.6
CO_2 ppm	978	631	506	1322	b.d.	722	297	788	b.d.	298
Olivine (Fo%)	87.7	85.3	86.4	85.0	82.2	82.5	88.0	84.5	82.9	84.9
% ol added	16.6	9.5	11.1	8.0	0.0	6.4	8.6	11.6	5.9	4.3
ΔT (°C)	188	105	110	73	1	92	68	153	64	49

Uncorrected	BRVB-01				J1d		P506		
	18.3	24-2	31-3	37-1	14.1	20.1	1.1	7.1	12.1
SiO_2	47.89	48.58	48.17	47.18	49.77	49.88	52.46	51.21	51.68
TiO_2	1.69	1.57	1.51	1.51	0.92	0.86	1.03	1.01	1.03
Al_2O_3	19.49	17.82	18.00	19.19	20.83	19.39	19.98	20.23	19.22
FeO^T	8.05	7.31	7.45	8.51	5.56	6.11	6.07	7.10	7.91
MnO	0.13	0.11	0.12	0.14	0.08	0.09	0.13	0.12	0.13
MgO	5.08	5.87	6.64	5.44	4.21	6.32	3.91	3.61	4.37
CaO	10.68	10.74	10.37	10.24	10.08	9.57	8.36	8.45	8.09
Na_2O	4.15	4.23	3.87	4.08	4.86	4.67	5.12	4.24	4.47
K_2O	1.15	0.93	0.80	1.14	0.77	0.72	0.94	0.90	0.88
P_2O_5	0.51	0.47	0.46	0.49	0.32	0.29	0.34	0.36	0.35
H_2O	0.1	1.6	1.2	0.4	2.6	2.8	1.4	1.6	0.8
H_2O uncertainty	±0.01	±0.8*	±0.14	±0.04	±0.17	±0.3	±0.1*	±0.3	N/A
CO_2 ppm	608	b.d.	905	b.d.	532	654	328	794	509
CO_2 uncertainty	±43	N/A	±150	N/A	±100	±76	±18*	±61	N/A

Corrected	BRVB-01				J1d		P506		
	18.3	24.2	31.3	37.1	14.1	20.1	1.1	7.1	12.1
SiO_2	47.71	48.54	48.50	47.62	49.10	49.51	52.28	51.93	52.60
TiO_2	1.61	1.47	1.45	1.47	0.79	0.78	0.98	0.98	1.03
Al_2O_3	18.56	16.63	17.27	18.72	17.83	17.48	18.99	19.57	19.30
Fe_2O_3	1.75	1.64	1.51	1.72	1.05	1.06	1.13	0.96	1.08
FeO	7.82	8.06	8.14	8.00	6.74	6.75	6.36	6.47	6.28
MnO	0.15	0.14	0.14	0.16	0.10	0.11	0.15	0.13	0.13
MgO	6.67	8.19	8.08	6.72	10.58	10.51	6.05	6.41	5.72
CaO	10.20	10.08	9.99	10.01	8.71	8.69	7.99	8.22	8.14
Na_2O	3.95	3.95	3.71	3.98	4.17	4.21	4.87	4.10	4.49
K_2O	1.10	0.87	0.77	1.12	0.66	0.65	0.90	0.87	0.88
P_2O_5	0.48	0.43	0.44	0.48	0.27	0.26	0.32	0.35	0.35
H_2O	0.1	1.5	1.1	0.4	2.2	2.4	0.0	1.5	0.8
CO_2 ppm	579	b.d.	858	b.d.	445	575	307	753	507
Olivine (Fo%)	83.9	86.1	85.7	83.7	90.8	90.7	85.4	85.6	84.6
% ol added	5.7	8.7	6.0	4.2	18.4	12.2	6.4	6.2	1.8
ΔT (°C)	58	71	40	43	209	116	85	112	53

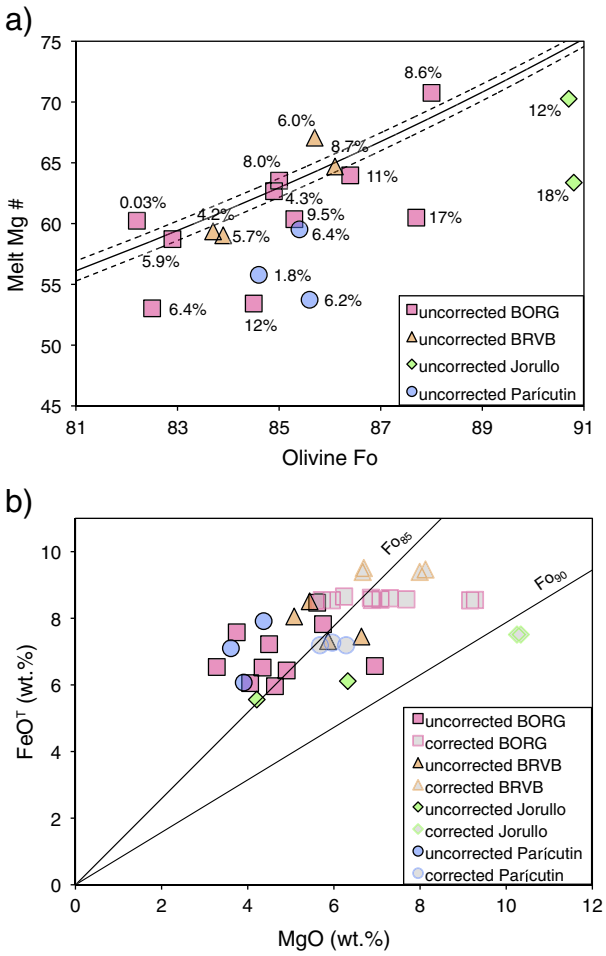

Fig. 2. (a) Uncorrected Mg# [Mg# = 100 (Mg^{2+} / (Mg^{2+} + Fe^{2+}))] compared to the Fo-content of the olivine host. The solid black curve shows the equilibrium relationship between corrected melt inclusion compositions and their olivine hosts for a K_d value of 0.3, which was the average calculated by Petrolog3. Dashed black curves show the range of K_d values (0.29–0.31). Percent values indicate the amount of olivine added back into each melt inclusion to restore it to equilibrium with its olivine host. Corrected melt inclusion compositions (not shown) would all plot within the two dashed curves. (b) Comparison of uncorrected (heavy shading) and corrected (light shading) FeO^T and MgO in melt inclusions. Black lines show values that are in equilibrium with Fo_{85} and Fo_{90} olivine.

3. Results

3.1. Host olivine and melt compositions

BORG olivine compositions are $Fo_{82.2}$–Fo_{88} (avg. $Fo_{84.9}$; Fig. 2a). BRVB olivines are similar, with an average of $Fo_{84.9}$ and a range of $Fo_{83.7}$–$Fo_{86.1}$. For Parícutin, three analyzed olivine grains have an average of $Fo_{85.2}$, with a range of $Fo_{84.6}$–$Fo_{85.6}$. The Fo contents for Parícutin are on the low end of the range of Fo contents reported in Johnson et al. (2009). Jorullo olivines have the most Mg-rich compositions of the samples we studied. The two Jorullo olivines analyzed in this study have compositions of $Fo_{90.7}$ and $Fo_{90.8}$. These values are similar to olivine from this same sample analyzed by Johnson et al. (2008, 2009).

The analyzed and corrected MgO and FeO^T contents of the melt inclusions are shown in Fig. 2b. The corrected MgO values range from 5.7 to 10.3 wt.% MgO, reflecting the range of host olivine compositions. On average, Jorullo melt inclusions showed the greatest amount of post-entrapment crystallization (15.3 wt.% olivine added), whereas Parícutin experienced the least (avg. of 4.8 wt.% olivine added). The average amount of PEC for BORG melt inclusions was 8.2 wt.% olivine, and for BRVB, 6.1 wt.%.

3.2. Raman CO_2 densities

A total of 415 bubbles were analyzed by Raman spectroscopy. Out of the 143 bubbles from BRVB, 67 have detectable CO_2 (i.e., the Fermi diad is recognizable in the Raman spectrum). Failure to detect CO_2 in a bubble does not necessary mean that the bubble does not contain CO_2. The ability to detect CO_2 in the vapor bubble is a function of the CO_2 density, the bubble size, the depth of the bubble beneath the mineral surface, the shape of the melt inclusion, the optical quality of the sample, and other factors. Moreover, it is possible that a given bubble that does not show detectable CO_2 did contain CO_2 initially, but it was subsequently lost along fractures. After background corrections, 47 of the 67 bubbles exhibited CO_2 peaks that could be fitted using the peak fitting software and background corrections. Some spectra could not be fit because they contained a high signal-to-noise ratio or because there was a high fluorescence background in the spectrum. Of the 143 bubbles analyzed, 10 Raman spectra had peaks that correspond to carbonate phases in the spectra. For BORG, of 249 analyzed bubbles, 96 had Raman spectra with observable CO_2 peaks, and 48 of these peaks could be fitted. Of the 249 analyzed bubbles, 55 had peaks that correspond to carbonate phases in their Raman spectra. We analyzed 54 bubbles from Parícutin, of which 18 show CO_2 peaks, and 10 could be fitted. No analyzed bubbles from Parícutin show peaks that correspond to carbonate phases in the spectra. We analyzed 81 bubbles from Jorullo, of which 29 have detectable CO_2, and 18 could be fitted. Of the 81 bubbles analyzed from Jorullo, 36 Raman spectra show peaks that correspond to carbonate phases.

Although there is considerable overlap in the data, measured CO_2 densities for several of the cinder cones show distinct differences (Fig. 3). Melt inclusions from BRVB have the highest CO_2 densities, ranging from 0.07 to 0.29 g/cm^3 (avg. 0.18 g/cm^3). BORG has slightly lower CO_2 densities, ranging from 0.05 g/cm^3 to 0.24 g/cm^3 (avg. 0.14 g/cm^3). Parícutin melt inclusions have the lowest CO_2 densities, ranging from 0.02 g/cm^3 to 0.12 g/cm^3 (avg. 0.06 g/cm^3). Jorullo melt inclusions contain bubbles with CO_2 densities of 0.03 g/cm^3 to 0.21 g/cm^3 (avg. 0.13 g/cm^3). CO_2 densities in bubbles with detectable carbonate have similar (BRVB) or lower (Jorullo) CO_2 densities compared to bubbles in melt inclusions from the same volcano but without a carbonate phase.

3.3. H_2O and CO_2 concentrations

To reconstruct the original dissolved CO_2 concentrations of the melt inclusions at the time of trapping, the amount of CO_2 in the melt

Notes to Table 2
Major element compositions of melt inclusion glass determined by electron microprobe analysis. Values are normalized to 100% without volatiles. Major element and H_2O concentrations are expressed in wt.%, and CO_2 concentrations are in ppm. H_2O and CO_2 values below FTIR detection limit are denoted "b.d.". "% ol added" is the amount of olivine added back into the melt inclusion to correct for post-entrapment crystallization using Petrolog3. Petrolog3 was used to calculate the eruptive temperature and trapping temperature for each inclusion: ΔT is the difference between the trapping and eruptive temperature (see discussion in Section 4.1). One standard deviation uncertainties for major elements, based on replicate analyses of each inclusion, are 0.24 wt.% for SiO_2, 0.03 wt.% for TiO_2, 0.18 wt.% for Al_2O_3, 0.12 wt.% for FeO^T, 0.01 wt.% for MnO, 0.24 wt.% for MgO, 0.05 wt.% for CaO, 0.18 wt.% for Na_2O, 0.02 wt.% for K_2O, and 0.01 wt.% for P_2O_5. Uncertainties in H_2O and CO_2 concentrations were calculated through error propagation as detailed in Section 2.3; uncertainties for melt inclusions that were corrected for olivine interference are shown with an asterisk. For standards, we used synthetic TiO_2 for Ti; synthetic MnO for Mn; NBS K-412 mineral glass for Al; NBS K-411 mineral glass for Fe, Ca, Si, and Mg; chlor-apatite (halogen corrected) for P; nepheline for Na; and orthoclase MAD-10 for K. Time dependent intensity corrections were made for Na, K, Si and Al. FeO and Fe_2O_3 for corrected compositions were calculated in Petrolog3 using an oxygen fugacity of QFM + 1.

inclusion glass must be known. However, to measure the concentrations of H_2O and CO_2 in the glass by FTIR spectroscopy requires that the melt inclusion diameter is >~30 μm. For melt inclusions smaller than 30 μm in diameter, we estimated the amount of CO_2 and H_2O in the glass using the median CO_2 and H_2O values for analyzed melt inclusions from the same sample (Johnson et al., 2008, 2009; Walowski, 2015; Walowski et al., 2016). A potential drawback to this approach is that smaller melt inclusions are likely to lose more H_2O by H^+ diffusive loss than larger melt inclusions because of their larger surface to volume ratio, and therefore the published H_2O values might be higher than many of the inclusions we analyzed by Raman. However, the H_2O content of the inclusion plays no role in the Raman-based restoration procedure (see below), so this should have no effect on our calculations of the CO_2 concentration. For BRVB, the median H_2O concentration is 1.7 wt.% with a median CO_2 of 538 ppm. For BORG, the median H_2O concentration is 2.9 wt.% with a median CO_2 concentration of 937 ppm. For samples from Jorullo, the median H_2O concentration is 3.0 wt.% and the median CO_2 concentration is 630 ppm. For Parícutin, the median H_2O concentration is 4.5 wt.% and the median CO_2 concentration is 850 ppm. We used the median CO_2 values to approximate the CO_2 concentrations of the glass in melt inclusions that were too small to analyze by FTIR, but for which we have measured vapor bubble CO_2 densities.

Twenty-nine inclusions from this study were large enough for FTIR analysis. For BORG, 13 analyzed melt inclusions yield CO_2 concentrations ranging from below detection (~25 ppm) to 1443 ppm (median 725 ppm). BORG melt inclusion H_2O ranges from 0.7 to 2.4 wt.% (median 1.5 wt.%). For six analyzed BRVB inclusions, CO_2 concentrations range from below detection (~25 ppm) to 905 ppm (median 613 ppm). The H_2O concentrations for BRVB range from 0.1 to 1.6 wt.% (median 0.74 wt.%). For Jorullo, four inclusions have CO_2 concentrations ranging from 532 to 897 ppm (median 683 ppm) with H_2O concentrations ranging from 0.6 to 2.8 wt.% (median 2.22 wt.%). Finally, the six FTIR-analyzed Parícutin melt inclusions have CO_2 concentrations ranging from 328 to 1136 ppm (median 512 ppm) with H_2O concentrations ranging from 0.8 to 1.6 wt.% (median 1.4 wt.%).

4. Discussion

4.1. Post-entrapment formation of vapor bubbles

The volume fraction occupied by a vapor bubble in a melt inclusion is strongly dependent on the extent of post-entrapment crystallization and thermal contraction of the melt phase relative to the contraction of the olivine host (Riker, 2005; Steele-MacInnis et al., 2011; Moore et al., 2015; Wallace et al., 2015). However, a crystallizing phenocryst can also trap melt that already contains one or more bubbles. To determine which bubbles may have formed in the melt prior to melt inclusion entrapment, we used the method of Riker (2005) to estimate the maximum volume fraction of vapor that could form in melt inclusions from each volcano as a result of post-entrapment crystallization and thermal contraction. This calculation allows us to identify melt inclusions that likely contain pre-entrapment bubbles and exclude them from our CO_2 reconstruction procedures, because these bubbles (which contained CO_2-rich vapor prior to melt inclusion entrapment) would cause an overestimate of the amount of CO_2 that was dissolved in the melt inclusion at the time of trapping.

For the bubble volume calculations, we assumed that there are two stages in the post-entrapment formation and growth of a bubble. The first stage occurs during post-entrapment cooling before eruption. It involves both olivine crystallization (which changes melt composition) and changes in the density of the included melt due to temperature decrease. The size of a bubble formed during this stage is therefore a function of ΔT, the difference between the eruption and trapping temperatures of the melt inclusion (Anderson and Brown, 1993; Riker, 2005; Wallace et al., 2015). The second stage occurs over short timescales (seconds to a few tens of seconds at most) during eruptive

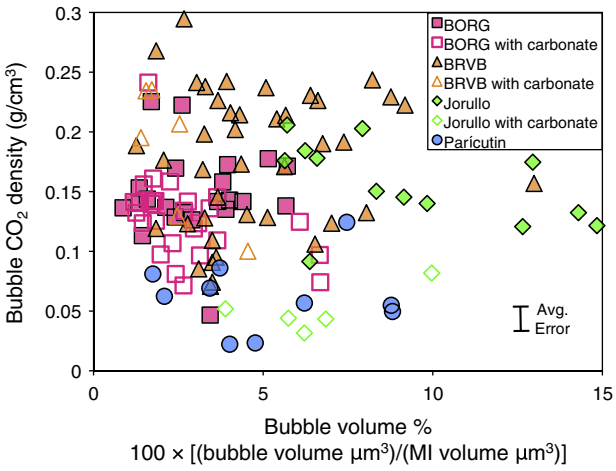

Fig. 3. Comparison of the volume percent vapor bubble in the melt inclusion and the vapor bubble CO_2 density as determined by Raman spectroscopy. CO_2 densities in bubbles with detectable carbonate are similar to (e.g. BORG) or lower (e.g. Jorullo) than CO_2 densities in bubbles without carbonate. The error bar shows the average uncertainty of the CO_2 density values (±0.02 g/cm^3; 1 standard deviation).

cooling and involves thermal contraction of the melt during cooling to the glass transition temperature. This second stage likely occurs too rapidly for additional olivine crystallization to occur, but may result in a significant increase in bubble volume.

To simulate the growth of a vapor bubble as a result of cooling, we first identified the most primitive melt composition (high MgO) for each volcano based on analyzed inclusions from this study as well as those analyzed previously from the same sample suites (Johnson et al., 2009; Walowski, 2015; Walowski et al., 2016). We used the highest H_2O/K_2O ratio and the K_2O content of the most primitive melt from each cone to estimate the H_2O content for the primitive melt composition (e.g. Johnson et al., 2010). Pre-eruption and trapping temperatures (based on analyzed and restored melt inclusion compositions, respectively; see Wallace et al., 2015) for each primitive composition were obtained using Petrolog3 (see Fig. B1 in Appendix B). The pressure of crystallization was calculated using the H_2O content paired with highest measured CO_2 in VolatileCalc 2.0 (Newman and Lowenstern, 2002).

We modeled the first stage of post-entrapment bubble formation using rhyolite-MELTS (Gualda et al., 2012). To simulate equilibrium crystallization (in 20 °C increments), each primitive melt composition was modeled with decreasing temperature below its liquidus at constant pressure. For each temperature step, we used the mass and density of olivine that crystallized in that step to calculate the volume change of a melt inclusion during cooling and crystallization. We calculated the density of the residual melt at each temperature step using the method of Lange and Carmichael (1990). We also calculated the volume decrease of the cavity containing the melt inclusion caused by olivine host contraction. (Suzuki, 1975). The volume difference between the cavity and the melt plus post-entrapment olivine crystallized at each sub-liquidus temperature step is then equal to the volume of a vapor bubble formed as a result of post-entrapment crystallization. One important result of these calculations is that during this stage of post-entrapment crystallization, the vapor bubble forms solely due to the volume change caused by crystallization of olivine from the included melt. The residual melt in the melt inclusion actually becomes less dense with decreasing temperature because of decreasing melt MgO and FeO and increasing melt H_2O caused by crystallization of olivine, and this compositional effect more than offsets the melt contraction effect due to cooling alone. So, the melt density decreases during this step, but the amount of melt decreases as a result of the loss of material from the melt during post-entrapment crystallization of olivine.

For the second (eruptive) stage of bubble expansion, we calculated the changes in melt and olivine density from the pre-eruptive

temperature to the glass transition temperature, at which point we assume any further bubble expansion ceases. For clarification, the pre-eruptive temperature corresponds to the last temperature of equilibration or near-equilibration between melt inclusion and host just before eruption and rapid quenching. During the eruptive cooling stage, we assumed that the olivine and melt compositions did not change, but we note that this is likely to be an oversimplification (Newcombe et al., 2014). Glass transition temperatures are dependent on H_2O content and were calculated using a relationship between H_2O and the onset of the glass transition temperature (°C) based on data in Giordano et al. (2005).

The results of these calculations allow us to place an upper limit on the size of bubbles that could have formed post-entrapment. A comparison of the calculations with our sample data suggests that most of the analyzed bubbles likely formed as a result of post-entrapment crystallization and thermal contraction of the melt phase (Fig. 4). Melt inclusions with bubbles that are larger than the calculated maximum bubble volume fraction were excluded from final CO_2 reconstructions, because these may be bubbles that were present in the melt before entrapment and were co-entrapped with melt into a melt inclusion. Comparing melt inclusion volume to bubble volume (Fig. 1) shows that the majority of melt inclusions for each volcano have similar volume percent bubbles. This suggests that most of the bubbles in the melt inclusions are the result of post-entrapment crystallization and thermal contraction of the melt phase rather than bubbles that were co-entrapped with melt. The results shown in Fig. 4 provide evidence that the melts at Jorullo, Parícutin, and BRVB were vapor saturated at the time of trapping, because some inclusions from each volcano appear to have formed by co-trapping of both melt and vapor. This is the best current method for distinguishing bubbles that were co-entrapped with the melt, because Fig. 3 shows that CO_2 density alone cannot be used to distinguish co-entrapped bubbles (large bubbles have similar CO_2 densities as smaller bubbles).

4.2. Restoration of melt inclusion CO_2 concentrations using measured CO_2 densities

The CO_2 concentrations in the melt inclusions at the time of trapping (before vapor bubble formation) can be calculated using the Raman-measured CO_2 densities, the glass CO_2 concentrations, the volume of the bubbles, and the volume of the melt inclusions. The sources of uncertainty in this calculation are in the determination of the bubble volume, the measured CO_2 density, and the dissolved concentration of CO_2 in the glass. Estimated uncertainty in volume % is 8–50% relative standard deviation (RSD) (median 17% RSD); uncertainty in measured CO_2 density is 9.7% RSD (based on repeat Raman analyses of a BRVB inclusion); and uncertainty in measured CO_2 ranges 5–52% RSD (median 17% RSD). Given that most of the bulk CO_2 in an inclusion is in the vapor bubble, the contribution from the uncertainty in dissolved CO_2 in the glass is small compared to the uncertainty in the mass of CO_2 in the bubble. As such, error in the Raman-reconstructed method was calculated using only the error in bubble CO_2 density and error in volume % bubble. Estimated uncertainties in the restored CO_2 values vary from $\pm$12 to 51% RSD, with a median value of $\pm$20% RSD. For those inclusions that were analyzed by FTIR for dissolved H_2O and CO_2, the reconstructions indicate that 40–90% [avg. 66 $\pm$ 17% (1 σ SD)] of the CO_2 originally

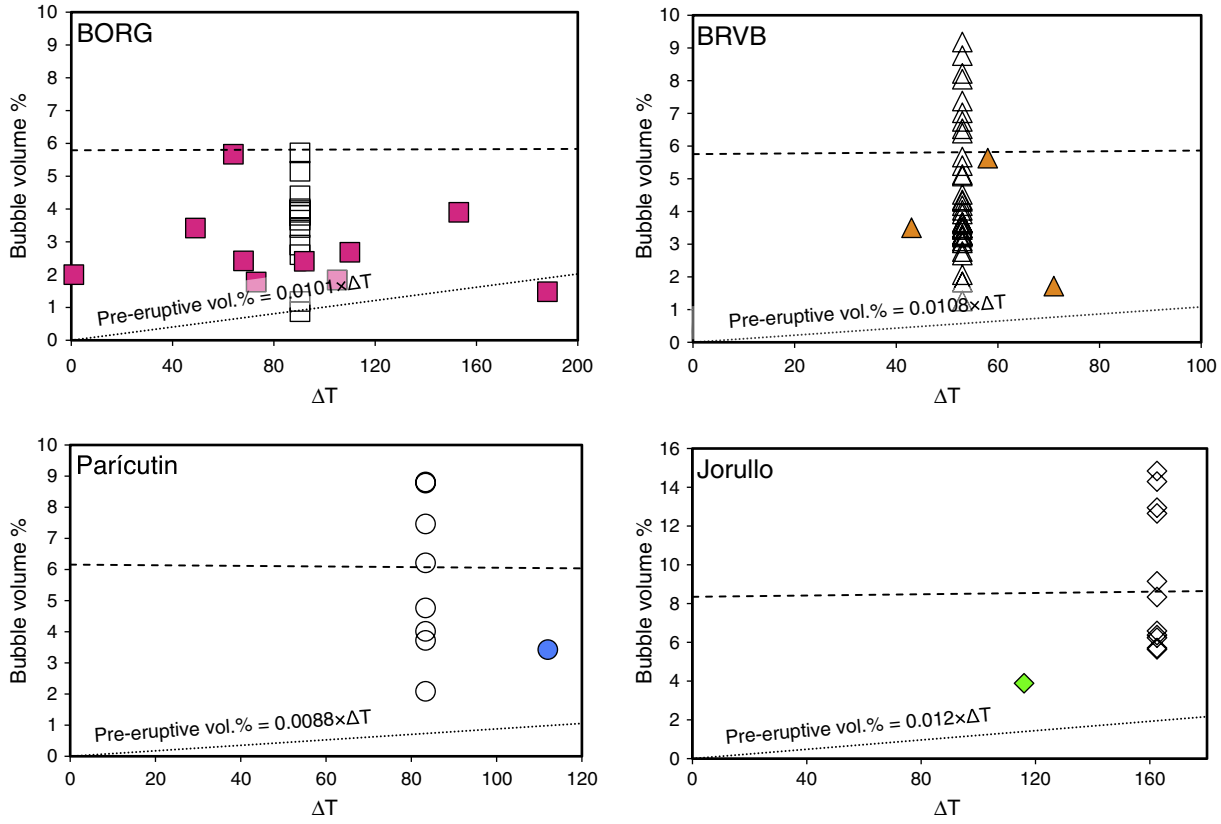

Fig. 4. Relationship between ΔT (the difference between melt inclusion trapping and eruption temperatures) and the maximum volume percent bubble formed as a result of cooling and crystallization for each volcano studied. The dotted line shows the volume percent bubble formed during pre-eruptive cooling and crystallization. The dashed line includes the effect of cooling and contraction down to the glass transition temperature during rapid eruptive cooling and quenching. Bubbles formed by post-entrapment processes should plot between the upper and lower lines because cooling during eruption may be too rapid compared to the relaxation time of the melt for the bubble to completely expand. Solid symbols represent bubbles in melt inclusions that were analyzed by electron microprobe. Open symbols represent bubbles in melt inclusions that were not analyzed by electron microprobe; for these, the average major element composition of other melt inclusions from the same volcano was used to estimate ΔT. Symbols plotting above the dashed line represent inclusions that likely trapped a vapor bubble along with the melt at the time of trapping. These melt inclusions and bubbles were not used in melt inclusion CO_2 reconstructions.

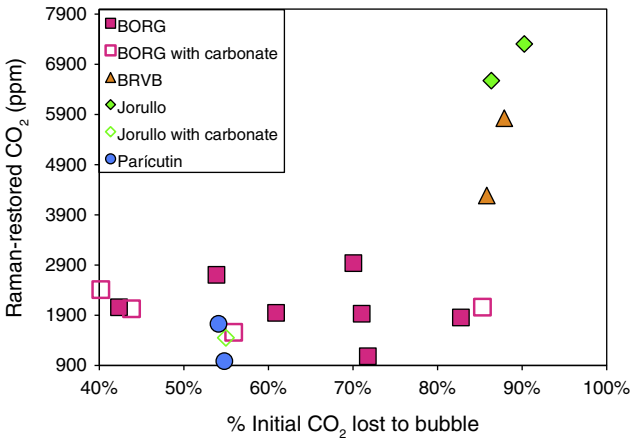

Fig. 5. Raman-restored CO_2 concentrations for each melt inclusion vs. the percent of initial dissolved CO_2 that was lost to the vapor bubble. Data are shown only for melt inclusions for which we were able to measure both CO_2 density in the bubble (from Raman analysis) and CO_2 concentrations in the glass (from FTIR analysis). These inclusions provide the best estimates of restored melt inclusion CO_2 concentrations because no assumptions were made concerning either CO_2 density or CO_2 concentrations in the glass.

in the melt inclusion was lost to the vapor bubble post-entrapment (Fig. 5). These values are similar to what has been found for melt inclusions from other basaltic eruptions (Esposito et al., 2011; Hartley et al., 2014; Moore et al., 2015; Wallace et al., 2015; Mironov et al., 2015). In general, the restored CO_2 does not depend on the fraction of initial dissolved CO_2 that was lost by post-entrapment bubble formation, though there are four melt inclusions with very high restored CO_2 that also have some of the greatest extents of CO_2 loss. For smaller inclusions that could not be analyzed by FTIR, we used the median dissolved CO_2 of other analyzed inclusions from the same cinder cone. The Raman results for the small inclusions suggest that 30–90% of initial dissolved CO_2 is contained in the bubble, comparable to the values given above for melt inclusions in which the glass CO_2 was analyzed by FTIR (Fig. 6).

4.3. Reconstruction of melt inclusion CO_2 concentrations using a cooling and crystallization model

For comparison with the CO_2 reconstructions based on the Raman data, we also estimated the original CO_2 concentrations of the melt inclusions using the results of the bubble formation model discussed above. This method is based on the approach used by Anderson and Brown (1993; see also Riker, 2005; Wallace et al., 2015). In this model, the volume fraction of the pre-eruptive bubble is estimated

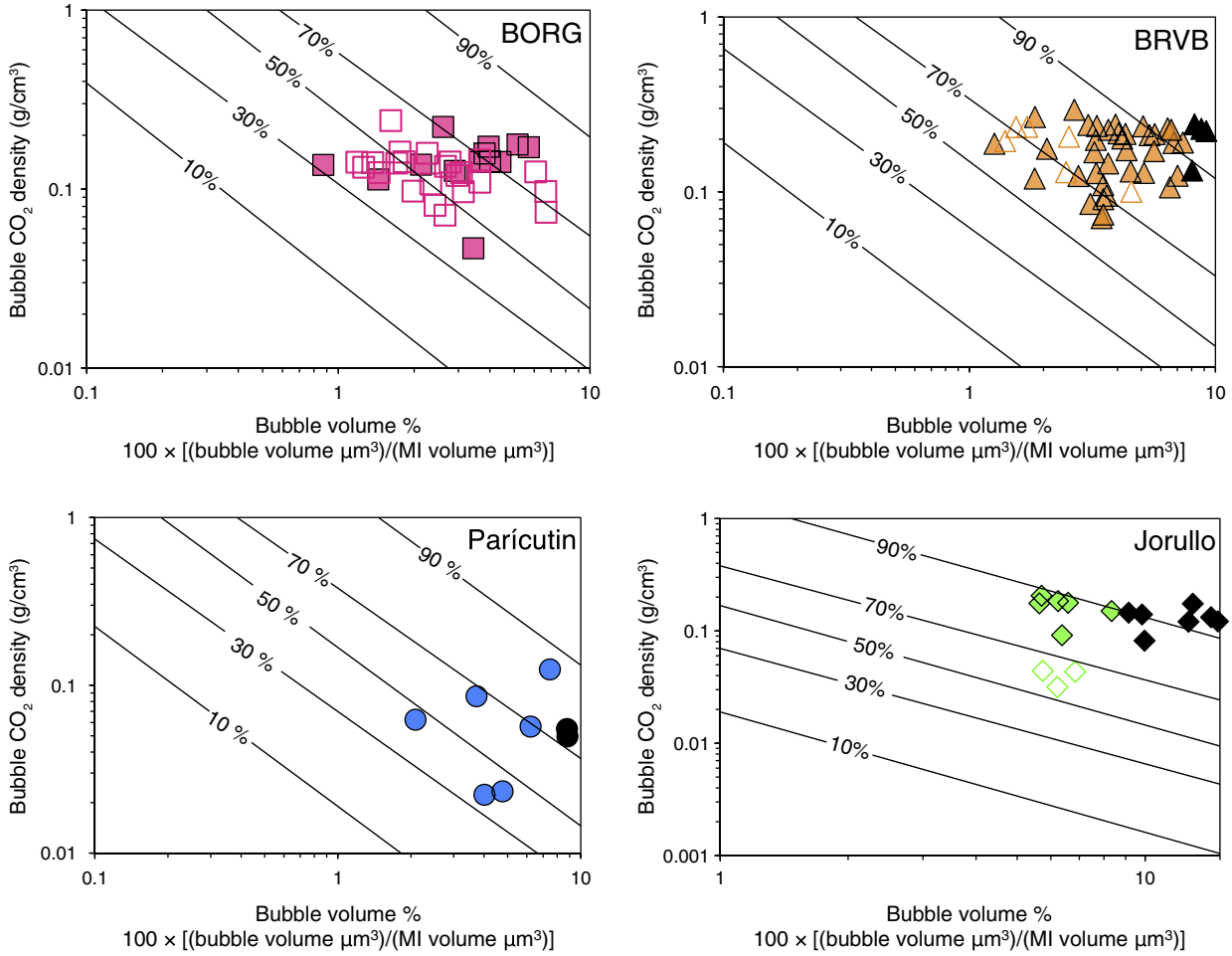

Fig. 6. Comparison of volume percent vapor bubble and Raman-measured CO_2 density for melt inclusions that were too small to analyze by FTIR (<30 µm in diameter). For these melt inclusions, the median CO_2 concentration of other analyzed inclusions from the same volcano was used to estimate the CO_2 concentration in the glass. Black lines represent the proportion of CO_2 (in weight percent) that was originally dissolved in the melt inclusion that was lost to the vapor bubble. Open symbols represent bubbles in which a carbonate phase was detected during Raman analysis. Black symbols show bubbles with a volume proportion that exceeds the maximum volume proportion calculated for bubbles from that volcano (see Section 4.1 and Fig. 4): These bubbles may have been co-entrapped along with the melt phase, and therefore they were not used in CO_2 reconstructions. The melt inclusion CO_2 reconstructions suggest that ~30–90% of CO_2 initially dissolved in the melt is contained in the bubble.

using the temperature difference between trapping and eruption (ΔT in Fig. 4). The composition of the vapor phase is then calculated using the solubility relations of Iacono-Marziano et al. (2012). Using this vapor composition, the mass of CO_2 in the vapor can be calculated and then added to the measured dissolved CO_2. This provides a model-restored, melt inclusion CO_2 concentration. The main sources of uncertainty in the model-restored CO_2 concentrations are in the estimated bubble volume, internal pressure in the inclusion at the time of eruption, and the dissolved concentration of CO_2 in the glass. Uncertainties in bubble volume and pressure are both estimated to be ~10% RSD, and uncertainty in dissolved CO_2 (as previously noted) is 5–52% RSD (median 17% RSD). Estimated uncertainties in the model-restored CO_2 values vary from 14 to 53% RSD, with a median value of 20% RSD.

An important assumption in this approach is that CO_2 is lost from the melt to the vapor bubble only during the pre-eruptive cooling and crystallization stage because the eruptive expansion stage occurs on a sufficiently short timescale that appreciable CO_2 cannot diffuse into the bubble (Wallace et al., 2015). To test this assumption, and to explore the timescales of CO_2 and H_2O diffusion from the melt in a melt inclusion to a vapor bubble, a one-dimensional model for diffusion as a result of an isothermal, instantaneous pressure drop was developed. The model calculates dissolved H_2O and CO_2 concentrations in the melt as a function of time and distance from the inclusion-bubble interface. Because both the diffusivity of H_2O (D_{H_2O}) and the diffusivity of CO_2 (D_{CO_2}) depend on the concentration of H_2O, we used a diffusion equation for both H_2O and CO_2 that considered the derivative of the diffusivity as a function of distance from the bubble:

$$\frac{dC}{dt} = \frac{dD}{dx}\cdot\frac{dC}{dx} + D\frac{d^2C}{dx^2} \quad (3)$$

where C is the concentration, t is time, D is the diffusivity, and x is the distance from the melt inclusion-bubble interface. For one of the two boundary conditions, we assume local equilibrium; at each timestep the composition at the vapor-melt interface is updated according to the new bubble composition (further information and the complete code are in Aster, 2015). At the other end of the model domain we use a no-flux boundary condition. The model uses an equation for the diffusivity of H_2O given in Zhang et al. (2007):

$$D_{H_2O} = C_{H_2O}\exp\left(-8.56-\frac{19110}{T}\right) \quad (4)$$

and an equation for the diffusivity of CO_2 formulated in Lloyd et al. (2014):

$$D_{CO_2} = \exp\left(-13.99-\frac{17367+1944.8P}{T}+\frac{855.2+271.2P}{T}\times C_{H_2O}\right) \quad (5)$$

where D_{H_2O} and D_{CO_2} are the diffusivities of H_2O and CO_2 (m^2/s), C_{H_2O} is the concentration of H_2O (wt.%), T is the temperature (K), and P is the pressure (GPa).

To assess the timescale of CO_2 loss to a vapor bubble, we started with a pressure of 3000 bars and then decreased the pressure to 2000 bars (ΔP = 1000 bars) or 1000 bars (ΔP = 2000 bars) at a temperature of 1150 °C. This represents the pressure drop that would occur due to cooling and crystallization. The starting pressure of 3000 bars is approximately in the middle of the range of pressures for BORG melt inclusions from this study after CO_2 reconstructions, and the ending pressures of 2000 and 1000 bars are two possible end pressures representing the range of pressures based on the analyzed concentrations of H_2O and CO_2 in the melt inclusion. We ran these simulations for model domains of 40 μm (the average BORG melt inclusion diameter) and 100 μm (the maximum BORG melt inclusion diameter). Because the vapor bubble is commonly not located in the center of the inclusion, the inclusion diameter represents a maximum diffusion distance relevant to the one-dimensional model. All models assumed a 10 μm diameter bubble (an average diameter for BORG bubbles), a H_2O concentration of 1.5 wt.% (an average analyzed H_2O concentration for BORG melt inclusions), and an initial CO_2 concentration sufficient to cause vapor saturation at the starting pressure. In the simulations, chemical equilibrium is reached when the last node (at the inclusion-crystal interface) is 99% re-equibrated. We then ran the code over shorter timescales, using the area above the diffusion profile divided by the area above the diffusion profile at equilibrium to calculate % re-equilibration. The results show that the melt and vapor reach equilibrium after ~6 min for a 40 μm inclusion and after ~36 min for a 100 μm inclusion (Fig. 7a). This indicates that if post-entrapment but pre-eruption cooling and crystallization occur on timescales longer than ~6 to 36 min, the bubble will reach equilibrium with the melt.

To estimate the amount of CO_2 that can be lost to the bubble during eruption, we ran several simulations of isothermal CO_2 loss to bubbles at temperatures of 1000 °C, 950 °C, 850 °C, 750 °C, and 650 °C (Fig. 7b). We undertook this approach because we lack knowledge of the cooling rate experienced by the melt inclusions. We also neglect bubble expansion during eruption as the melt rapidly cools to the glass transition temperature. The results of this approach suggest that if eruptive cooling and quenching occur on timescales of ~10–20 s (e.g., see Anderson and

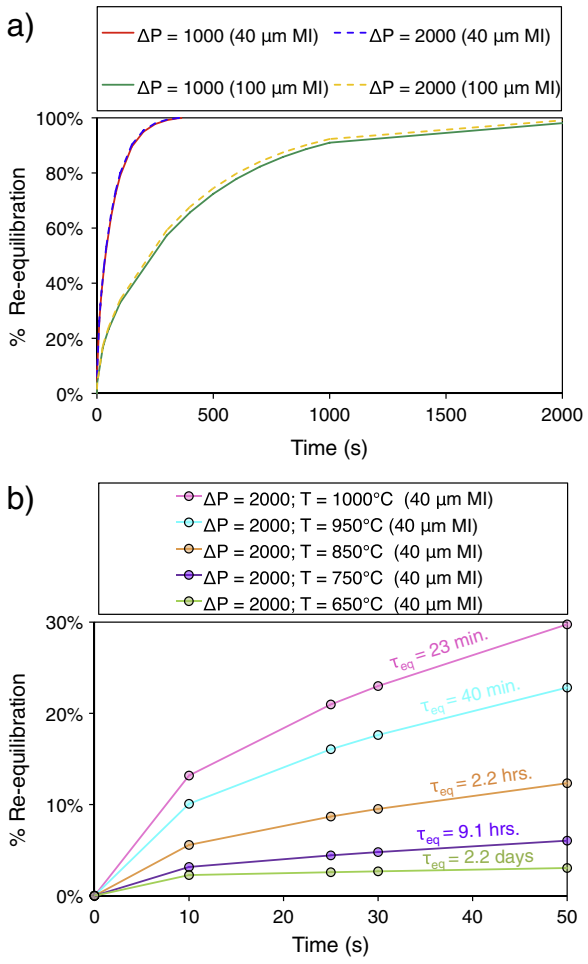

Fig. 7. (a) Diffusive re-equilibration of CO_2 between melt and vapor bubble for diffusion lengths of 40 μm and 100 μm. In (a) we assume a constant temperature of 1150 °C and an instantaneous pressure drop from 3000 bars to 2000 bars (ΔP = 1000 bars) and 3000 bars to 1000 bars (ΔP = 2000 bars). (b) The percent re-equilibration of CO_2 between melt and vapor bubble during eruption at temperatures of 1000 °C, 950 °C, 850 °C, 750 °C, and 650 °C. Data labels indicate the equilibration time (τ_{eq}) calculated for each temperature, and data points show the time steps for which % re-equilibration was calculated. During the short timescales (10 s of seconds) of eruptive cooling, CO_2 diffusion into the bubble is insignificant. As temperature quickly approaches the glass transition temperature, a negligible amount of CO_2 likely diffuses into the bubble.

Brown, 1993, discussion of cooling of tephra in fire fountains), only limited re-equilibration of melt and vapor will occur (Fig. 7b). As temperatures rapidly decrease from ~1000 °C to the glass transition temperature (~450 °C), a cooling rate of 1–10 °C/s is expected to lead to limited to negligible re-equilibration.

4.4. Comparison of Raman and bubble formation model results

A comparison of the two independent methods that we used to estimate the original CO_2 concentrations of melt inclusions at the time of trapping is shown in Fig. 8a and Table 3. For the purpose of comparison, we refer to the two methods as Raman-restored and model-restored. Many melt inclusions show reasonably good agreement between the two methods, and for 10 of 17 inclusions, the two methods are within ±550 ppm CO_2 (avg. difference 290 ppm), equivalent to ±~300 bars uncertainty in estimated trapping pressure for restored inclusions. Most melt inclusions that showed Raman evidence for a carbonate phase in the bubble or no detectable CO_2 during Raman analysis of the bubble show higher model-restored values than Raman-restored values, as expected. For such inclusions, Raman-restored values likely underestimate the amount of CO_2 in the bubble because the amount of CO_2 in carbonate crystals is excluded from the reconstruction, and failure to detect CO_2 in vapor bubbles does not necessarily mean that the bubbles are CO_2-free, for reasons described above. A subset of the melt inclusions has distinctly higher Raman-restored values than model-restored values. All of these melt inclusions have anomalously low H_2O compared to other inclusions from the same samples (Fig. 8b). This suggests that these inclusions may have been affected by post-entrapment diffusive H^+ loss, which leads to an underestimate of the original CO_2 content during modeling because loss of H^+ causes the pre-eruption bubble to be larger than it would be due to crystallization and cooling alone (e.g., Bucholz et al., 2013). The alternative possibility that these melt inclusions are inclusions that trapped melt plus a vapor bubble is not supported by the comparison of the bubble sizes with the maximum calculated pre-eruption bubble (see Fig. 4). Our results thus show that for inclusions that have lost substantial H^+ by diffusion, a more reliable estimate of the original CO_2 content of the melt is provided by the Raman method (compared to the crystallization model) because the Raman method directly measures the density of CO_2 in the vapor bubble.

Our results clearly support and confirm earlier studies showing that subduction-related basaltic magmas have relatively high CO_2 concentrations. Restored values from our dataset (Fig. 10) have upper limits in the range of 3000–3500 ppm CO_2 (BORG), 4500–6000 ppm (BRVB), 1800 ppm (Parícutin), and 6500–7500 ppm (Jorullo). Estimates for other arc volcanoes range up to 4000 ppm CO_2 (Fuego; Moore et al., 2015; Raman method) and 3800 ppm (Klyuchevskoy; Mironov et al., 2015; experimental rehomogenization of melt inclusions). These values

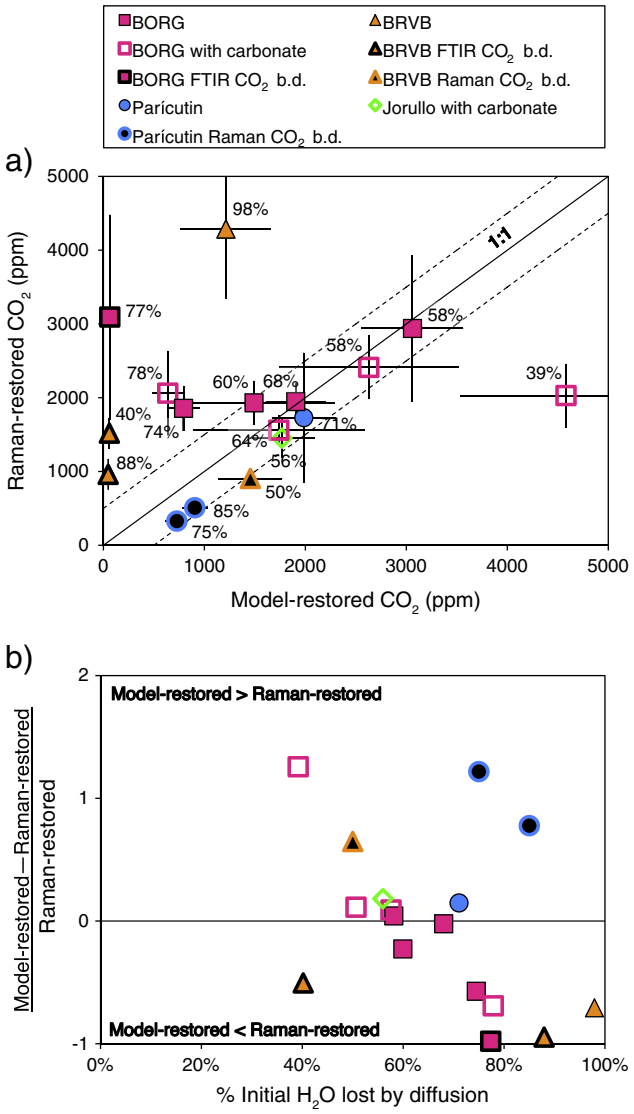

Fig. 8. (a) Comparison of restored melt inclusion CO_2 concentrations predicted by the cooling and crystallization model (horizontal axis) and melt inclusion CO_2 concentrations restored by measuring CO_2 density in the bubble by Raman spectroscopy and then adding that CO_2 back into the glass (vertical axis). Black line indicates 1:1 relationship, and dashed lines represent ±500 ppm CO_2. Data labels indicate the percent of initial H_2O that we infer to have been lost by H^+ diffusion based on a comparison of H_2O/K_2O values for melt inclusions from a given volcano. (b) Estimated extent of diffusive H^+ loss (expressed as % of initial H_2O lost) vs. the difference between the Raman and crystallization models for CO_2 restoration. Melt inclusions plotting above the black line have higher model-restored CO_2 values than Raman-restored CO_2 values, whereas melt inclusions plotting below the black line have higher Raman-restored CO_2 values than model-restored CO_2 values. Melt inclusions that lost a large amount of H_2O have higher model-restored CO_2 values than Raman-restored CO_2 values. Note that the two Parícutin inclusions that deviate strongly from the trend of the other inclusions are ones in which CO_2 in the bubbles was below detection. Thus the Raman method likely underestimates restored CO_2 for these inclusions.

Table 3
Raman-restored CO_2 and model-restored CO_2 concentrations.

Sample	Raman-rest. CO_2 (ppm)	Raman-rest. CO_2 uncertainty RSD (%)	Model-rest. CO_2 (ppm)	Model-rest. CO_2 uncertainty RSD (%)
BORG (BORG-1)				
5.2	2030	23	4581	23
19.2	1561	13	1737	49
19.5	1931	15	1492	53
19.8	2411	18	2628	34
23.1	1948	12	1905	16
24.1	1856	16	794	20
27.2	2939	34	3061	16
32.a	3094	45	63	23
33.3	2062	28	637	24
BRVB (BRVB-01)				
18.3	4286	22	1213	37
24.2	1520	15	59	14
31.3[a]	905	–	1455	22
37.1	961	22	47	14
Jorullo (J1d)				
20.1	1452	18	1768	18
Paricutin (P506)				
1.1[a]	328	–	727	15
7.1	1729	51	1984	16
12.1[a]	509	–	905	14

Uncertainty is reported % relative standard deviation (RSD).
[a] For three inclusions, there was no detectable CO_2 in the bubble; the values reported for Raman-restored CO_2 concentrations for these three inclusions are the dissolved CO_2 in glass values determined by FTIR, and no uncertainty is given.

are comparable to an estimate of >3000 ppm dissolved CO_2 in arc magmas inferred from CO_2 emissions from arc volcanoes (Wallace, 2005).

4.5. Hydrogen loss and H_2O reconstructions

It has been shown experimentally that diffusive H^+ (proton) loss from melt inclusions in olivine can occur on timescales as short as an hour (Danyushevsky et al., 2002; Massare et al., 2002; Gaetani et al., 2012; Lloyd et al., 2013; Bucholz et al., 2013). To explore the extent to which diffusive H^+ loss from melt inclusions might have contributed to vapor bubble formation in our study, we estimated the magnitude of potential H_2O loss. To do this, we assumed that the highest H_2O/K_2O values for melt inclusions from each volcano are representative of melt inclusions before any diffusive H^+ loss. Then for each melt inclusion we were able to estimate the H_2O concentration before any diffusive loss and compare it to the actual measured value. This method should give us an upper limit for diffusive loss from each melt inclusion because it is possible that melt inclusions were trapped from already partially degassed melt (e.g., see Metrich and Wallace, 2008; Lloyd et al., 2013), whereas our approach assumes that they were all trapped from undegassed melts. For melt inclusions for which we had no electron microprobe data but did have FTIR data, we assumed the average value of K_2O concentration for analyzed inclusions from the same volcano to estimate the original H_2O concentration.

The estimated extent of diffusive H_2O loss for each melt inclusion is compared to measured bubble volume percent in Fig. 9. Although there is considerable scatter in the data, the results suggest that H^+ loss is linked to the growth of large bubbles in melt inclusions from these sample suites. This is consistent with the pattern shown in Fig. 8b, which shows that inclusions that have been the most strongly affected by diffusive H^+ loss have restored CO_2 concentrations that are strongly underpredicted by our cooling and crystallization model.

The results in Fig. 9 suggest that all the melt inclusions we analyzed have been affected by H^+ loss to varying degrees, though we emphasize again that our estimates are upper limits for how much diffusive loss might have occurred. Many of the inclusions we analyzed have H_2O values that are lower than the median H_2O values of inclusions from the same samples analyzed in previous studies (Johnson et al., 2009; Walowski, 2015; Walowski et al., 2016). The melt inclusions analyzed in previous studies were chosen to be large enough for FTIR analysis, whereas the inclusions selected in this study encompassed many smaller inclusions because they were initially selected for Raman analysis. Thus our sample set contained more smaller inclusions, which is likely the cause of greater H^+ diffusive loss in our inclusions.

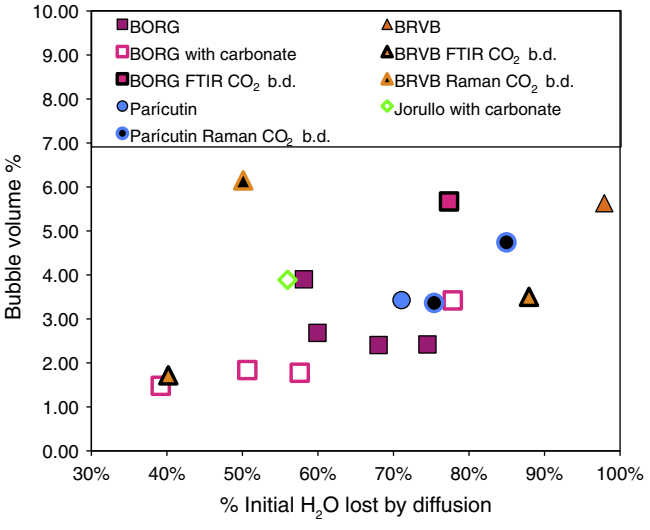

Fig. 9. Estimated extent of diffusive H^+ loss (expressed as % of initial H_2O lost) vs. volume percent vapor bubble in the inclusion. The positive correlation suggests that large bubbles formed as a result of diffusive H^+ loss. The starting H_2O concentration was calculated using H_2O/K_2O ratios as described in Section 4.5. The highest H_2O/K_2O ratios for each volcano were as follows: Jorullo, 8.8; Parícutin, 6.2; BRVB, 2.9; BORG, 6.4.
Data from Johnson et al. (2009); Walowski (2015); Walowski et al. (2016).

4.6. Melt inclusion trapping pressures

We used the reconstructed H_2O and CO_2 concentrations to estimate the original trapping pressures of the melt inclusions and to examine the extent to which post-entrapment bubble formation and diffusive H^+ loss result in lower apparent pressures. Vapor saturation pressures (Fig. 10) were calculated using the solubility relations of Iacono-Marziano et al. (2012) and Papale et al. (2006). Using the analyzed dissolved H_2O and CO_2 concentrations of the melt inclusions, vapor saturation pressures range from 164 to 2080 bars for BORG, 62 to 1065 bars for BRVB, 886 to 1350 bars for Parícutin, and 1072 to 1333 bars for Jorullo. With Raman-corrected CO_2, the pressures are significantly higher, from 1529 to 3522 bars for BORG, 1249 to 5290 bars for BRVB, 1471 to 2257 bars for Parícutin, and 1962 to 5445 bars for Jorullo. After correcting for both CO_2 loss to the bubble and H^+ loss from the melt inclusion, the reconstructed pressures range from 2377 to 3917 bars for BORG, 1924 to 5074 bars for BRVB, 3552 to 4148 bars for Parícutin, and 2960 to 5513 bars for Jorullo. It should be emphasized that the H_2O corrections yield the maximum possible initial H_2O values, so the CO_2 and H_2O reconstructed values shown in Fig. 10 provide an upper limit for initial trapping pressures. Our results show that the decrease in CO_2 concentration in the melt (glass) that is caused by post-entrapment bubble formation has a significant effect on inferred pressure of trapping. Loss of H^+ by diffusion also affects the inferred trapping pressure, but to a lesser extent than does CO_2. This is because CO_2 solubility has a much stronger pressure-dependence than H_2O, so the CO_2 concentration is a more sensitive pressure indicator, especially for melt inclusions with a relatively low H_2O content.

5. Conclusions

The results of this study support a growing body of evidence that post-entrapment bubble formation in melt inclusions can dramatically decrease the concentration of dissolved CO_2 in the included melt. Our conclusion reiterates the importance of post-entrapment melt inclusion modification due to CO_2 diffusion into vapor bubbles and H^+ diffusion (effectively, H_2O loss) out of melt inclusions. As a result, estimates of melt inclusion entrapment pressures based on dissolved H_2O and CO_2 concentrations measured only in the glass phase will typically underestimate the true pressure of trapping, unless the melt inclusions are bubble free.

Our calculations of vapor bubble volume fractions as a function of ΔT (the difference between eruptive and trapping temperatures) show that during cooling and post-entrapment crystallization, melt density decreases so that pre-eruptive bubble growth is solely the result of the volume change caused by post-entrapment crystallization. During eruption, however, the melt in the inclusion thermally contracts more than the olivine host, causing pre-eruptive bubbles to expand greatly. We demonstrate with a model of H_2O and CO_2 diffusion that the timescales for this eruptive phase likely result in a negligible contribution of CO_2 to the vapor bubble, especially for larger inclusions.

We also show that the original concentration of dissolved CO_2 at the time of trapping can be established using densities of CO_2 in vapor bubbles obtained from Raman analysis, as well as by mass balance methods using calculated pre-eruptive bubble volumes. However, CO_2 reconstructions using these two methods can be complicated by the presence of carbonate crystals at the melt inclusion-bubble interface (effectively removing CO_2 from the vapor bubble and therefore decreasing CO_2 densities measured by Raman spectroscopy) and the diffusive loss of H^+ out of the melt inclusion (which increases the bubble volume fraction

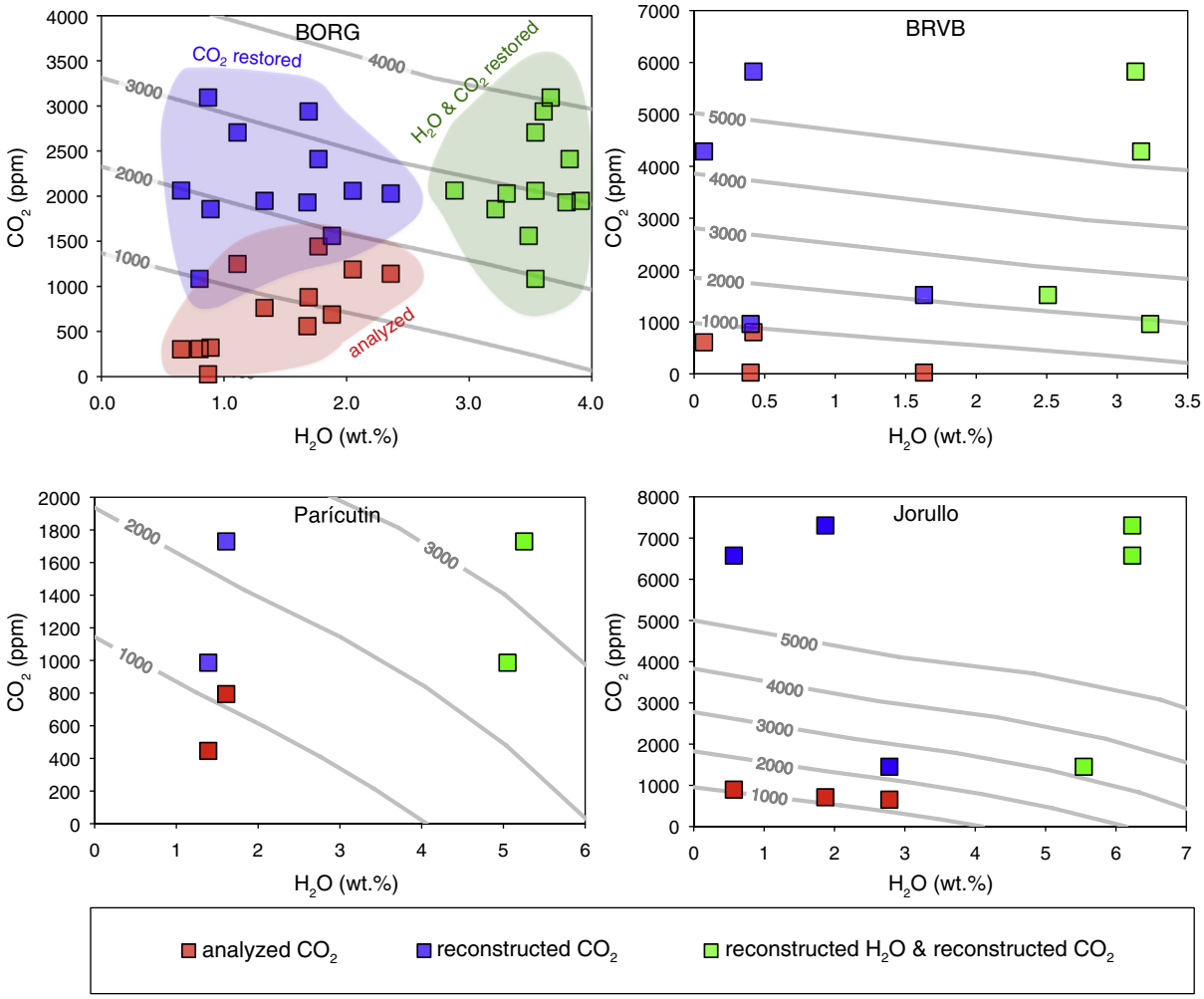

Fig. 10. Comparison of analyzed CO_2 and H_2O concentrations (red), corrected CO_2 and analyzed H_2O concentrations (blue), and corrected CO_2 concentrations and corrected (for diffusive H^+ loss) H_2O concentrations (green). Vapor saturation isobars (gray) were calculated using the model of Papale et al. (2006). For inclusions for which there was no FTIR data, we assumed 25 ppm dissolved CO_2 in the glass. The results show that trapping conditions based on volatile analysis of the glass only (not corrected for CO_2 loss to the vapor bubble) result in significantly underestimated trapping pressures. The effect of H_2O loss via diffusion on estimated trapping pressure is less severe. (For interpretation of the references to color in this figure legend, the reader is referred to the web version of this article.)

compared to what is calculated with the crystallization model). Thus, it is advisable that both methods be compared when reconstructing melt inclusion CO_2 concentrations. Furthermore, inclusions with very low H_2O concentrations compared to other melt inclusions from the same sample are suspect as low H_2O concentrations might reflect H^+ loss.

Acknowledgments

This work was supported by the National Science Foundation through grant EAR-1119224 to PJW and grant EAR-1249404 to JMW, as well as the Sara J. Staggs Undergraduate Transition Award to EMA from University of Oregon Women in Graduate Science. We would like to thank reviewers A. Lloyd and K. Iacovino for their thoughtful and thorough comments, and K. Walowski for providing unpublished data and performing Petrolog3 calculations. Lastly, thanks to C. Farley for assistance with the Raman analyses, as well as J. Donovan and J. Chouinard for their help during electron microprobe analysis.

Appendix A. Supplementary data

Supplementary data to this article can be found online at http://dx.doi.org/10.1016/j.jvolgeores.2016.04.028.

References

Abramoff, M.D., Magalhaes, P.J., Ram, S.J., 2004. Image processing with ImageJ. Biophoton. Int. 11 (7), 36–42.
Anderson, A.T., Brown, G.G., 1993. CO_2 contents and formation pressures of some Kilaueanmelt inclusions. Am. Mineral. 78, 794–803.
Aster, E., 2015. Reconstructing CO_2 Concentrations in Basaltic Melt Inclusions From Mafic Cinder Cones Using Raman Analysis of Vapor Bubbles (M.S. Thesis) University of Oregon.
Bucholz, C.E., Gaetani, G.A., Behn, M.D., Shimizu, N., 2013. Post-entrapment modification of volatiles and oxygen fugacity in olivine-hosted melt inclusions. Earth Planet. Sci. Lett. 374, 145–155.
Clynne, M.A., and Muffler, L.J.P., 2010. Geologic map of Lassen Volcanic National Park and vicinity, California: U.S. Geological Survey Scientific Investigations Map 2889, scale 1: 50,000.
Danyushevsky, L.V., 2001. The effect of small amounts of H_2O on crystallisation of mid-ocean ridge and backarc basin magmas. J. Volcanol. Geotherm. Res. 110 (3), 265–280.
Danyushevsky, L.V., Plechov, P., 2011. Petrolog3: integrated software for modeling crystallization processes. Geochem. Geophys. Geosyst. 12, Q07021. http://dx.doi.org/10.1029/2011GC003516.
Danyushevsky, L.V., Della-Pasqua, F.N., Sokolov, S., 2000. Re-equilibration of melt inclusions trapped by magnesian olivine phenocrysts from subduction-related magmas: petrological implications. Contrib. Mineral. Petrol. 138, 68–83.
Danyushevsky, L.V., McNeill, A.W., Sobolev, A.V., 2002. Experimental and petrological studies of melt inclusions in phenocrysts from mantle-derived magmas: an overview of techniques, advantages, and complications. Chem. Geol. 183, 5–24.
Dixon, J.E., Pan, V., 1995. Determination of the molar absorptivity of dissolved carbonate in basanitic glass. Am. Mineral. 80, 1339–1342.
Dixon, J.E., Stolper, E.M., Holloway, J.R., 1995. An experimental study of water and carbon dioxide solubilities in mid-ocean ridge basaltic liquids. Part 1: calibration and solubility models. J. Petrol. 36, 1607–1631.

Esposito, R., Bodnar, R.J., Danyushevsky, L.V., De Vito, B., Fedele, L., Hunter, J., Lima, A., Shimizu, N., 2011. Volatile evolution of magma associated with the Solchiaro eruption in the Phlegrean volcanic district (Italy). J. Petrol. 52 (12), 2431–2460.
Fall, A., Tattitch, B., Bodnar, R.J., 2011. Combined microthermometric and Raman spectroscopic technique to determine the salinity of H_2O–CO_2–NaCl fluid inclusions based on clathrate melting. Geochim. Cosmochim. Acta 75, 951–964.
Gaetani, G.A., O'Leary, J.A., Shimizu, N., Bucholz, C.E., Newville, M., 2012. Rapid equilibration of H_2O and oxygen fugacity in olivine-hosted melt inclusions. Geology 40, 915–918.
Giordano, D., Nichols, A.R.L., Dingwell, D.B., 2005. Glass transition temperatures of natural hydrous melts: a relationship with shear viscosity and implications for the welding process. J. Volcanol. Geotherm. Res. 142, 105–118.
Gualda, G.A.R., Ghiorso, M.S., Lemons, R.V., Carley, T.L., 2012. Rhyolite-MELTS: a modified calibration of MELTS optimized for silica-rich, fluid-bearing magmatic systems. J. Petrol. 53, 875–890.
Hartley, M.E., Maclennan, J., Edmonds, M., Thordarson, T., 2014. Reconstructing the deep CO_2 degassing behaviour of large basaltic fissure eruptions. Earth Planet. Sci. Lett. 393, 120–131.
Hauri, E., 2001. Sims analysis of volatiles in silicate glasses, 2: isotopes and abundances in Hawaiian melt inclusions. Chem. Geol. 183, 115–141.
Iacono-Marziano, G., Morizet, Y., Le Trong, E., Gaillard, F., 2012. New experimental data and semi-empirical parameterization of H_2O–CO_2 solubility in mafic melts. Geochim. Cosmochim. Acta 97, 1–23.
Johnson, E.R., Wallace, P.J., Cashman, K.V., Delgado Granados, H., 2010. Degassing of volatiles (H_2O, CO_2, S, Cl) during ascent, crystallization, and eruption at mafic monogenetic volcanoes in central Mexico. J. Volcanol. Geotherm. Res. 197, 225–238.
Johnson, E.R., Wallace, P.J., Cashman, K.V., Delgado Granados, H., Kent, A.J.R., 2008. Magmatic volatile contents and degassing-induced crystallization at Volcano Jorullo, Mexico: implications for melt evolution and the plumbing systems of monogenetic volcanoes. Earth Planet. Sci. Lett. 269, 477–486.
Johnson, E.R., Wallace, P.J., Granados, H.D., Manea, V.C., Kent, A.J.R., Bindeman, I.N., Donegan, C.S., 2009. Subduction-related volatile recycling beneath Central Mexico: insights from melt inclusions, oxygen isotopes, and geodynamic models. J. Petrol. 50, 1729–1764.
Lange, R.L., Carmichael, I.S.E., 1990. Thermodynamic properties of silicate liquids with emphasis on density, thermal expansion, and compressibility. Rev. Mineral. 24, 25–59.
Lloyd, A.S., Plank, T., Ruprecht, P., Hauri, E.H., Rose, W., 2013. Volatile loss from melt inclusions in pyroclasts of differing sizes. Contrib. Mineral. Petrol. 165 (1), 129–153.
Lloyd, A.S., Ruprecht, P., Hauri, E.H., Rose, W., Gonnermann, H.M., Plank, T., 2014. NanoSIMS results from olivine-hosted melt embayments: magma ascent during explosive basaltic eruptions. J. Volcanol. Geotherm. Res. 283, 1–18.
Lowenstern, J.B., 1995. Application of silicate-melt inclusions to the study of magmatic volatiles. In: Thompson, J.F.H. (Ed.), Magmas, Fluids and Ore Deposits, pp. 71–100.
Luhr, J.F., 2001. Glass inclusions and melt volatile contents at Parícutin Volcano, Mexico. Contrib. Mineral. Petrol. 142, 261–283.
Mallmann, G., O'Neill, H.S.C., 2009. The crystal/melt partitioning of V during mantle melting as a function of oxygen fugacity compared with some other elements (Al, P, Ca, Sc, Ti, Cr, Fe, Ga, Y, Zr and Nb). J. Petrol. 50 (9), 1765–1794.
Massare, D., Métrich, N., Clocchiatti, R., 2002. High-temperature experiments on silicate melt inclusions in olivine at 1 atm: inference on temperatures of homogenization and H_2O concentrations. Chem. Geol. 183 (1), 87–98.
Metrich, N., Wallace, P.J., 2008. Volatile abundances in basaltic magmas and their degassing paths tracked by melt inclusions. Minerals, Inclusions, and Volcanic Processes, Reviews in Mineralogy and Geochemistry Vol. 69. Mineralogical Society of America, pp. 363–402.
Mironov, N., Portnyagin, M., Botcharnikov, R., Gurenko, A., Hoernle, K., Holtz, F., 2015. Quantification of the CO_2 budget and H_2O-CO_2 systematics in subduction-zone magmas through the experimental hydration of melt inclusions in olivine at high H_2O pressure. Earth Planet. Sci. Lett. 425, 1–11.
Moore, L.R., Gazel, E., Tuohy, R., Lloyd, A.S., Esposito, R., Steele-Macinnis, M., Hauri, E.R., Wallace, P.J., Plank, T., Bodnar, R.J., 2015. Bubbles matter: an assessment of the contribution of vapor bubbles to melt inclusion budgets. Am. Mineral. 100 (4), 806–823.
Newcombe, M.E., Fabbrizio, A., Zhang, Y., Ma, C., Le Voyer, M., Guan, Y., Eiler, J.M., Saal, A.E., Stolper, E.M., 2014. Chemical zonation in olivine-hosted melt inclusions. Contrib. Mineral. Petrol. 168 (1), 1–26.
Newman, S., Lowenstern, J.B., 2002. VolatileCalc: a silicate melt–H_2O–CO_2 solution model written in Visual Basic for Excel. Comput. Geosci. 28 (5), 597–604.
Nichols, A.R.L., Wysoczanski, R.J., 2007. Using micro-FTIR spectroscopy to measure volatile contents in small and unexposed inclusions hosted in olivine crystals. Chem. Geol. 242 (3–4), 371–384.
Papale, P., Moretti, R., Barbato, D., 2006. The compositional dependence of the saturation surface of H_2O + CO_2 fluids in silicate melts. Chem. Geol. 229, 78–95.
Riker, J., 2005. The 1859 eruption of Mauna Loa Volcano, Hawaii: Controls on the development of long lava channels. Unpublished M.S. Thesis, University of Oregon.
Roedder, E., 1979. Origin and significance of magmatic inclusions. Bull. Mineral. 102, 467–510.
Sorby, H.C., 1858. On the microscopic structure of crystals, indicating the origin of minerals and rocks. Geol. Soc. London Q. Jord. 14 (1), 453–500.
Steele-MacInnis, M., Esposito, R., Bodnar, R.J., 2011. Thermodynamic model for the effect of post-entrapment crystallization on the H_2O–CO_2 systematics of vapor-saturated, silicate melt inclusions. J. Petrol. 52, 2461–2482.
Sterner, S.M., Bodnar, R.J., 1984. Syntehtic fluid inclusions in natural quartz I. Compositional types synthesized and applications to experimental geochemistry. Geochim. Cosmochim. Acta 48, 2659–2668.
Student, J.J., Bodnar, R.J., 1996. Melt inclusion microthermometry: petrologic constraints from the H_2O-saturated haplogranite system. Petrology 4 (3), 291–306.
Suzuki, I., 1975. Thermal expansion of periclase and olivine, and their anharmonic properties. J. Phys. Earth 23, 145–159.
Wallace, P.J., 2005. Volatiles in subduction zone magmas: concentrations and fluxes based on melt inclusion and volcanic gas data. J. Volcanol. Geotherm. Res. 140 (1), 217–240.
Wallace, P.J., Kamenetsky, V.S., Cervantes, P., 2015. Melt inclusion CO_2 contents, pressures of olivine crystallization, and the problem of shrinkage bubbles. Am. Mineral. 100 (4), 787–794.
Walowski, K., 2015. From Cinder Cones to Subduction Zones: Volatile Recycling and Magma Formation Beneath the Southern Cascade Arc (Dissertation) University of Oregon.
Walowski, K.J., Wallace, P.J., Clynne, M.A., Rasmussen D.J., Weis D. (2016) Slab melting and magma formation beneath the southern Cascade arc. Earth Planet. Sci. Lett., (in review).
Wright, R.B., Wang, C.H., 1973. Density effect on the Fermi resonance in gaseous CO_2 Raman scattering. J. Chem. Phys. 58, 2893–2895.
Wright, R.B., Wang, C.H., 1975. Effect of density on the Raman scattering of molecular fluids. II. Study of intermolecular interactions in CO_2. J. Chem. Phys. 61, 2707–2710.
Wysoczanski, R., Tani, K., 2006. Spectroscopic FTIR imaging of water species in silicic volcanic glasses and melt inclusions: an example from the Izu-Bonin arc. J. Volcanol. Geotherm. Res. 156 (3–4), 302–314.
Zhang, Y., Zhengjiu, X., Zhu, M., Wang, H., 2007. Silicate melt properties and volcanic eruptions. Rev. Geophys. 45, RG4004.